K2-260 b: A hot Jupiter transiting an F star, and K2-261 b: A warm Saturn around a bright G star

Monthly Notices of the ROYAL ASTRONOMICAL SOCIETY

MNRAS **481,** 596–612 (2018) doi:10.1093/mnras/sty2238
Advance Access publication 2018 August 16

K2-260 b: a hot Jupiter transiting an F star, and K2-261 b: a warm Saturn around a bright G star

M. C. Johnson,[1★] F. Dai,[2,3] A. B. Justesen,[4] D. Gandolfi,[5] A. P. Hatzes,[6] G. Nowak,[7,8] M. Endl,[9] W. D. Cochran,[9] D. Hidalgo,[7,8] N. Watanabe,[10] H. Parviainen,[7,8] T. Hirano,[11,12] S. Villanueva, Jr,[1†] J. Prieto-Arranz,[7,8] N. Narita,[8,13,14,15,16] E. Palle,[7,8] E. W. Guenther,[6] O. Barragán,[5] T. Trifonov,[17] P. Niraula,[18] P. J. MacQueen,[9] J. Cabrera,[19] Sz. Csizmadia,[19] Ph. Eigmüller,[19] S. Grziwa,[20] J. Korth,[20] M. Pätzold,[20] A. M. S. Smith,[19] S. Albrecht,[4] R. Alonso,[7,8] H. Deeg,[7,8] A. Erikson,[19] M. Esposito,[6] M. Fridlund,[21,22] A. Fukui,[14] N. Kusakabe,[14,15] M. Kuzuhara,[14,15] J. Livingston,[23] P. Montañes Rodriguez,[7,8] D. Nespral,[7,8] C. M. Persson,[21] T. Purismo,[24] S. Raimundo,[25] H. Rauer,[19,26] I. Ribas,[27] M. Tamura,[13,14,15] V. Van Eylen[22] and J. N. Winn[3]

Affiliations are listed at the end of the paper

Accepted 2018 August 9. Received 2018 August 8; in original form 2018 April 4

ABSTRACT

We present the discovery and confirmation of two new transiting giant planets from the *Kepler* extended mission *K2*. K2-260 b is a hot Jupiter transiting a $V = 12.7$ F6V star in *K2* Field 13, with a mass and radius of $M_\star = 1.39^{+0.05}_{-0.06}$ $M_\odot$ and $R_\star = 1.69 \pm 0.03$ $R_\odot$. The planet has an orbital period of $P = 2.627$ d, and a mass and radius of $M_P = 1.42^{+0.31}_{-0.32}$ M_J and $R_P = 1.552^{+0.048}_{-0.057}$ R_J. This is the first *K2* hot Jupiter with a detected secondary eclipse in the *Kepler* bandpass, with a depth of 71 ± 15 ppm, which we use to estimate a geometric albedo of $A_g \sim 0.2$. We also detected a candidate stellar companion at 0.6 arcsec from K2-260; we find that it is very likely physically associated with the system, in which case it would be an M5-6V star at a projected separation of ∼400 au. K2-261 b is a warm Saturn transiting a bright ($V = 10.5$) G7IV/V star in *K2* Field 14. The host star is a metal rich ([Fe/H] = 0.36 ± 0.06), mildly evolved $1.10^{+0.01}_{-0.02}$ $M_\odot$ star with $R_\star = 1.65 \pm 0.04$ $R_\odot$. Thanks to its location near the main-sequence turn-off, we can measure a relatively precise age of $8.8^{+0.4}_{-0.3}$ Gyr. The planet has $P = 11.633$ d, $M_P = 0.223 \pm 0.031$ M_J, and $R_P = 0.850^{+0.026}_{-0.022}$ R_J, and its orbit is eccentric ($e = 0.39 \pm 0.15$). Its brightness and relatively large transit depth make this one of the best-known warm Saturns for follow-up observations to further characterize the planetary system.

Key words: planets and satellites: detection – planets and satellites: individual: K2-260 b, K2-261 b.

1 INTRODUCTION

Our knowledge of exoplanets has been revolutionized by the *Kepler* mission (Borucki et al. 2010), which during its prime mission discovered thousands of exoplanet candidates and confirmed exoplanets, providing powerful statistical measurements of planetary populations. After the failure of a second reaction wheel in 2013, the *Kepler* spacecraft began the *K2* extended mission (Howell et al. 2014), pointing at a succession of fields around the ecliptic for ∼80 d per field. The *K2* mission has resulted in the detection of over 200 confirmed and validated planets, and even more planet candidates, to date (e.g. Mayo et al. 2018). On average *K2* target stars are brighter than those from the *Kepler* prime mission, resulting in a population of planets that is more amenable to direct confirma-

★ E-mail: johnson.7240@osu.edu
† NSF Graduate Research Fellow.

tion, and further observations to characterize these systems in more detail.

Building a large sample of planets that are characterized in detail will help to move the field of exoplanet population statistics beyond the parameters that have been probed by *Kepler* (principally planetary radius and orbital period; e.g. Burke et al. 2015). Large statistical studies of planetary atmospheres, spin-orbit misalignments, and other properties measurable via follow-up observations promise to set much more powerful constraints upon models of planet formation, migration, and evolution, and illuminate planetary astrophysics in general (e.g. Morton & Johnson 2011; Sing et al. 2016).

Although a large number of planets and planet candidates around bright stars will soon be provided by the *Transiting Exoplanet Survey Satellite* (*TESS*; Ricker et al. 2015) mission, *K2* planets are complementary to those that will be found by *TESS*. *K2* observes in the ecliptic plane, which will not be covered by *TESS* during its prime mission. *K2* is thus helping *TESS* to complete an all-sky catalogue of transiting short-period planets around relatively bright stars. Additionally, as *K2* campaigns are significantly longer than *TESS* pointings (∼80 versus ∼27 d), *K2* is capable of finding longer-period planets than *TESS* typically will over most of the sky.

We present here the discovery, confirmation, and additional characterization of two new transiting planets from *K2*: K2-260 b and K2-261 b. K2-260 b is a hot Jupiter transiting a $V = 12.7$ mid-F star, while K2-261 b is a warm Saturn transiting a $V = 10.6$ late-G star near the main-sequence turn-off. Both are amenable to further observations, and can add to the number of giant planets characterized in detail.

These planets were discovered and characterized as part of the KESPRINT collaboration to find planets using *K2*. Our team has confirmed and characterized over two dozen transiting planets using *K2*, including hot Jupiters (e.g. Grziwa et al. 2016; Hirano et al. 2016b; Johnson et al. 2016), longer-period giant planets (e.g. Smith et al. 2017; Van Eylen et al. 2018), ultra-short-period planets (e.g. Dai et al. 2017; Smith et al. 2018), multiplanet systems (e.g. Gandolfi et al. 2017; Niraula et al. 2017), as well as other planets (e.g. Narita et al. 2017).

2 OBSERVATIONS

2.1 *K2* photometry

The *Kepler* spacecraft observed *K2* Field 13 from 2017 March 8 to May 27 UT, a span of 79.0 d. Field 13 is centred at RA = $04^{h}51^{m}11^{s}$, Dec. = $+20°47'11''$ (J2000.0). The star EPIC 246911830 (K2-260) was proposed for observations by programmes GO13122 (P.I. Howard) and GO13071 (P.I. Charbonneau). *K2* Field 14 was observed for 70.4d between 2017 May 31 and August 9 UT. Field 14 is centred at RA = $10^{h}42^{m}44^{s}$, Dec. = $+06°51'06''$ (J2000.0). EPIC 201498078 (K2-261) was proposed for observations by programmes GO14009 (P.I. Charbonneau), GO14020 (P.I. Adams), GO14021 (P.I. Howard), and GO14028 (P.I. Cochran).

We conducted three parallel searches of all of the light curves from Campaigns 13 and 14 for transits using three separate methodologies. One method utilizes aperture photometry to extract light curves from the *K2* raw pixel data and decorrelates the light curves based upon the centroid motion to account for the roll of the spacecraft, as described in Dai et al. (2016). We then perform a standard BLS (box least squares; Kovács, Zucker & Mazeh 2002) transit search upon the light curves.

The other two methods both used the *K2* light curves for Campaigns 13 and 14 as extracted and corrected for systematics per Vanderburg & Johnson (2014) as provided by A. Vanderburg.[1] We used the EXOTRANS package (Grziwa, Pätzold & Carone 2012) in order to search the light curves for transits. This package utilizes the VARLET (Grziwa & Pätzold 2016) wavelet-based filtering technique in order to remove stellar and systematic variability from the light curves, along with a BLS transit search algorithm. If a transit is detected, it is removed using another wavelet-based filtering technique, PHALET, and the light curve searched again for additional transits using BLS.

We also used the code DST (Cabrera et al. 2012) to search for transits in the Vanderburg & Johnson (2014) light curves. This algorithm is conceptually similar to BLS, but uses a more realistic transit shape rather than an inverted tophat for the transit search, accounts for the potential presence of transit timing variations, and uses improved statistical methods.

All three search techniques detected significant transits for both K2-260 (with a period of ∼2.6 d and a depth of ∼1 per cent) and K2-261 (with a period of ∼11.6 d and a depth of ∼0.3 per cent); indeed, the transits are easily visible by eye in the detrended *K2* light curves (Fig. 1). None of the algorithms identified any additional candidate transits for either star.

We list the coordinates, magnitudes, and other identifying information for K2-260 and K2-261 in Table 1.

2.2 High-resolution imaging

In order to test for the presence of nearby stars that could dilute the transit depth and perhaps indicate that the planet candidate could be a false positive, we obtained high-resolution imaging observations of both K2-260 and K2-261.

We obtained high-resolution images of K2-260 using the Infrared Camera and Spectrograph (IRCS; Kobayashi et al. 2000) with the adaptive optics (AO) system AO188: (Hayano et al. 2010) mounted on the 8.2 m Subaru telescope on 2018 March 29 UT. For the AO imaging, we adopted the fine-sampling mode (20 mas per pixel) and *H*-band filter. Short exposure, unsaturated frames (0.6 s × 3 co-adds for each position) were first secured with five-point dithering, which are used for the absolute flux calibration. We then ran long-exposure sequences (15 s × 3 co-adds for each position) adopting the same five-point dithering, resulting in saturated frames of K2-260 to look for faint nearby companions. The total exposure time amounted to 450 s for the saturated frames.

Following Hirano et al. (2016a), we applied dark subtraction, bad pixel interpolation, flat fielding, and distortion correction to the raw IRCS frames. The unsaturated and saturated frames were then respectively aligned and combined to obtain the final reduced images. The combined unsaturated image of K2-260 showed that the AO-corrected full width at half-maximum (FWHM) of the target's PSF was 0.10 arcsec.

Visual inspection of the combined saturated image suggested a presence of a faint source in the southeast of K2-260 with a separation of ∼0.6 arcsec (see the inset of Fig. 2). In order to estimate the contrast of this candidate companion (CC), we performed aperture photometry for K2-260 and its CC with its aperture radius being the FWHM of the target. For the CC's photometry, we applied high-pass filtering (with a width of 4 × FWHM) to the saturated image to suppress the halo of the primary star.

[1] https://www.cfa.harvard.edu/avanderb/k2.html

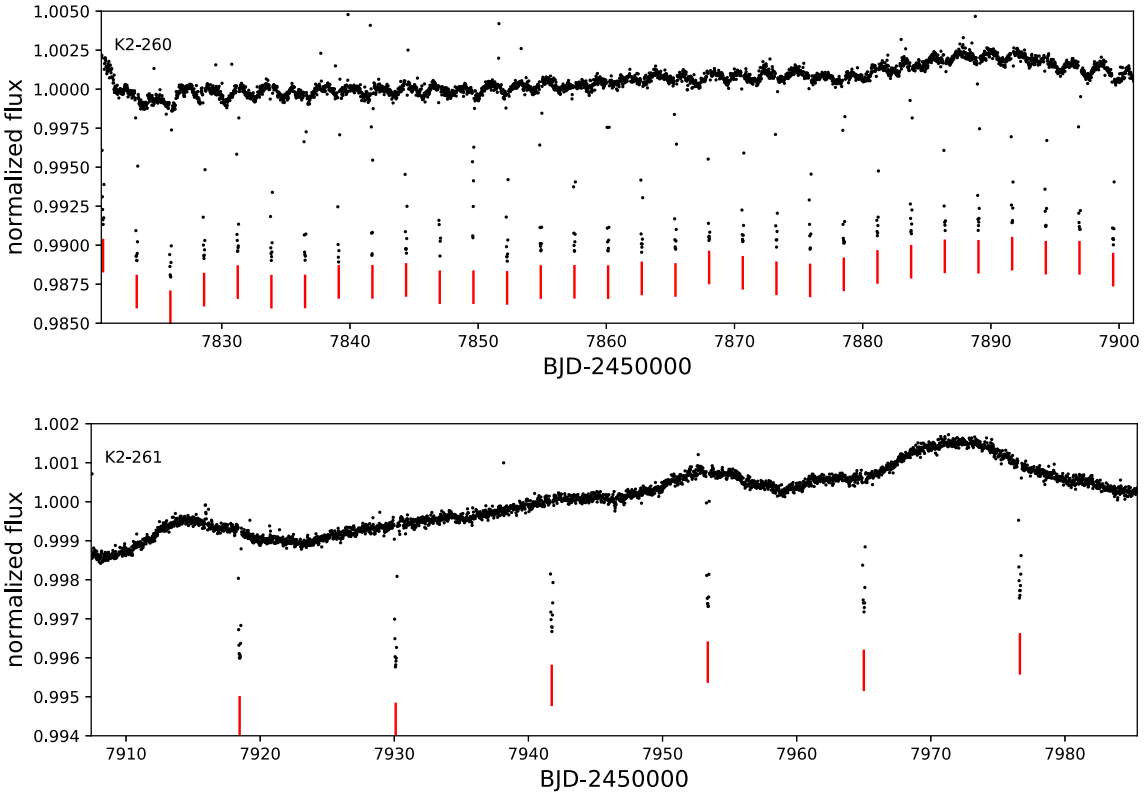

Figure 1. *K2* light curves of K2-260 (top), and K2-261 (bottom), as detrended and corrected for systematics by Vanderburg & Johnson (2015). Note the rotational variability of K2-260, which is discussed in Section 3.4. For both systems, we remove the stellar and instrumental variations prior to fitting the transits. Vertical bars mark the locations of each transit.

High-pass filtering suppresses the halo of the primary star, but it also reduces the CC's flux. In order to estimate the flux loss from the high-pass filtering, we implemented a simulation in which an artificial companion's signal is injected into the saturated image with the same angular separation (but with different position angles). The mock data were analysed using the same steps above to measure the artificial companion's flux. As a result, we found that approximately 25 per cent of the injected signal was lost by high-pass filtering. Taking into account this flux loss, we measured the CC's magnitude and its position. Table 2 summarizes the measured CC properties. To evaluate the detection level of the CC, we also drew the 5σ contrast curve based on the scatter of the flux count in the annulus as a function of angular separation from K2-260. Fig. 2 implies that at the separation of $\sim$0.6 arcsec, a 5σ contrast of $\Delta H = 7.3$ mag was achieved, and thus the CC was detected with $>5\sigma$.

The companion has a flux ratio of 0.00200 ± 0.00033, corresponding to $\Delta H = 6.75 \pm 0.18$ mag. It is located at an angular separation of 0.605 ± 0.026 arcsec and a position angle of $151.8^\circ \pm 2.5^\circ$. If the companion were to be physically associated with K2-260, this corresponds to a projected physical separation of 409 ± 21 au at the 676 pc distance of K2-260 (Gaia Collaboration et al. 2018).

We obtained the observations of K2-261 using the FastCam lucky imaging camera (Oscoz et al. 2008) on the 1.52 m Telescopio Carlos Sánchez at Teide Observatory, Spain. FastCam is a very low noise and fast readout speed electron multiplying CCD camera with 512×512 pixels (with a physical pixel size of 16 μm, and a field of view of 21.2×21.2 arcsec). We observed K2-261 on 2018 March 20 UT, obtaining 5000 individual frames with 50 ms exposure times through a clear filter. The conditions were clear with 1.7 arcsec seeing and we obtained a Strehl ratio of 0.06. In order to construct a high-resolution, long-exposure image, each individual frame was bias-subtracted, aligned, and co-added and then processed with the FastCam dedicated software (Labadie et al. 2010; Jódar et al. 2013). Fig. 3 shows the contrast curve that was computed based on the scatter within the annulus as a function of angular separation from the target centroid. We used a high-resolution image constructed by co-addition of the 30 per cent best images, so that it had a 75 s total exposure time, which achieved a 5σ detection limit better than $\sim$6 mag outside 3 arcsec separation, and better than $\sim$3 mag outside $\sim$50 mas. We did not detect any secondary sources within these limits inside 6.0 arcsec of K2-261.

2.3 Ground-based photometry

In order to perform additional false positive vetting of K2-260, we obtained follow-up ground-based photometric observations of several transits. We obtained these observations with two different facilities.

First, we observed with the DEMONEXT automated 0.51 m robotic telescope (Villanueva et al. 2018), located at Winer Observatory, Arizona, USA. We observed the transits of 2017 November 14 and 22 UT in alternating Sloan g and i filters, using 20 s exposures in each band, and binned together each set of five consecutive exposures in each band in order to increase the signal-to-noise ratio (SNR). We obtained these pseudo-simultaneous multiband observations in order to verify that the transit is achromatic, excluding certain blended eclipsing binary scenarios. The observations were obtained through thin clouds, degrading the expected photometric performance, but none the less we detect the transits of K2-260 b.

Table 1. Coordinates, magnitudes, and kinematics of K2-260 and K2-261.

Parameter	K2-260	K2-261	Reference
Coordinates and identifiers			
RA (J2000.0)	$05^{h}07^{m}28\overset{s}{.}16$	$10^{h}52^{m}07\overset{s}{.}78$	1
Dec. (J2000.0)	$+16°52'03\overset{''}{.}78$	$+00°29'36\overset{''}{.}07$	1
EPIC	246911830	201498078	–
TYC	–	255-257-1	–
UCAC4	535-011514	453-051151	–
2MASS	J05072816+1652037	J10520778+0029359	–
AllWISE	J050728.15+165203.7	J105207.76+002935.6	–
Magnitudes			
Kp (mag)	12.465	10.451	1
G (mag)	12.467	10.459	2
Bp (mag)	12.798	10.872	2
Rp (mag)	11.973	9.917	2
B (mag)	13.217 ± 0.042	11.561 ± 0.086	1
V (mag)	12.69 ± 0.11	10.612 ± 0.059	1
g (mag)	12.881 ± 0.010	10.979 ± 0.010	1
r (mag)	12.449 ± 0.030	10.402 ± 0.020	1
i (mag)	12.287 ± 0.010	10.226 ± 0.020	1
J (mag)	11.400 ± 0.023	9.337 ± 0.030	1
H (mag)	11.189 ± 0.032	8.920 ± 0.042	1
K (mag)	11.093 ± 0.021	8.890 ± 0.022	1
*W*1 (mag)	11.039 ± 0.023	8.828 ± 0.023	3
*W*2 (mag)	11.036 ± 0.021	8.897 ± 0.020	3
*W*3 (mag)	10.895 ± 0.129	8.819 ± 0.031	3
*W*4 (mag)	>9.006	>8.281	3
$B - V$ (mag)	0.53 ± 0.12	0.95 ± 0.10	4
$J - K$ (mag)	0.307 ± 0.031	0.447 ± 0.037	4
Distance and velocities			
μ_{RA} (mas yr^{-1})	0.667 ± 0.078	-23.664 ± 0.075	2
μ_{Dec} (mas yr^{-1})	-6.045 ± 0.051	-44.171 ± 0.068	2
Π (mas)	1.479 ± 0.042	4.660 ± 0.043	2
d (pc)	676 ± 19	214.6 ± 2.0	2
v_{rad} (km s^{-1})	29.1 ± 2.7	3.28 ± 0.52	2
U (km s^{-1})	15.8 ± 2.6	-8.99 ± 0.13	This work
V (km s^{-1})	-6.15 ± 0.57	-29.14 ± 0.49	This work
W (km s^{-1})	-9.46 ± 0.73	-21.81 ± 0.50	This work

Notes. The mean stellar radial velocity v_{rad} is measured from our FIES (FIbre-fed Échelle Spectrograph) spectra for K2-260 and from our McDonald reconnaissance spectrum for K2-261. The quoted *UVW* velocities are in the local standard of rest (LSR) frame and use the LSR definition and *UVW* frame of Coşkunolu et al. (2011). References: 1: Ecliptic Plane Input Catalog (EPIC: Huber et al. 2016; https://archive.stsci.edu/k2/epic/search.php); 2: *Gaia* DR2 (Gaia Collaboration et al. 2018); 3: AllWISE (Cutri et al. 2013); 4: calculated from literature values given earlier in this table.

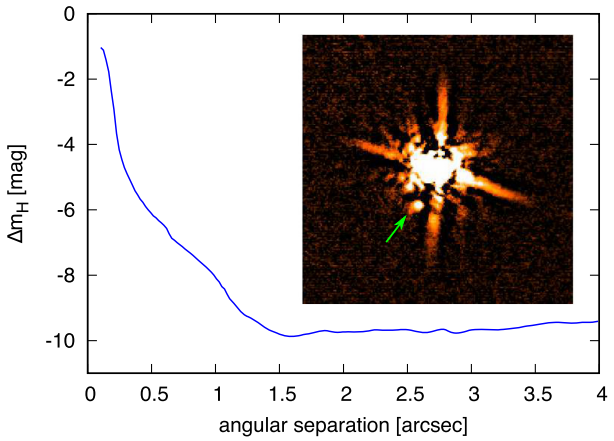

Figure 2. *H*-band 5σ contrast curve of K2-260 from IRCS. Inset: high-pass filtered image. The candidate companion is marked with an arrow.

Table 2. Properties of the candidate companion to K2-260.

Parameter	Unit	Value	Uncertainty
Measured parameters			
ρ	arcsec	0.605	0.026
PA	°	151.8	2.5
f_{CC}/f_A		0.002 00	0.000 33
ΔH	mag	6.75	0.18
Estimated parameters			
$a_\perp$	au	409	21
M_{CC}	$M_\odot$	0.145	0.015
Spec. type		M5-6V	

Notes. f_{CC}/f_A is the flux ratio of the companion with respect to the primary in the *H* band. $a_\perp$ is the projected separation.

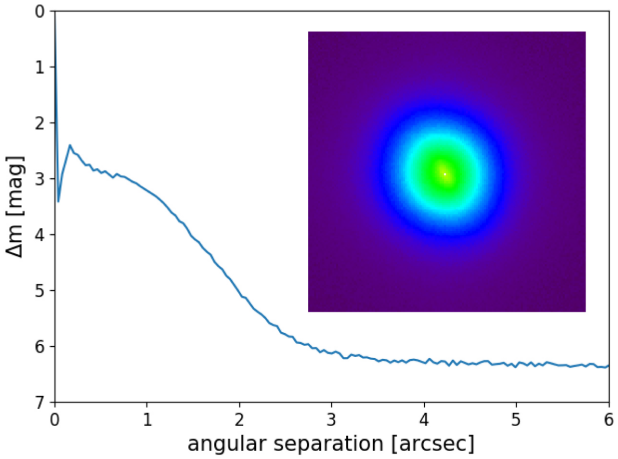

Figure 3. Clear filter contrast curve as a function of angular separation up to 6.0 arcsec from K2-261 obtained with the FastCam camera at TCS. The solid line indicates the 5σ detection limit for secondary sources, none of which are detected. The inset shows the 6×6 arcsec combined image of K2-261. North is up and east is left.

The transits in both *g* and *i* appear to be slightly shallower than that in the *K2* light curve; however, given the precision of the DEMONEXT data and systematic uncertainties in the depth associated with detrending the DEMONEXT data, we do not consider these differences to be significant. Furthermore, if these depth differences were due to dilution by another star, we would not expect *both* bands to exhibit smaller transit depths than the *K2* data unless the contaminating star were to be of a very similar $T_{\rm eff}$ to K2-260. Although the DEMONEXT data are much less precise than the *K2* photometry, we none the less include them in our fits (Section 3.3) as the longer time baseline improves the precision of our ephemeris measurement. We show these data in Fig. 6.

We additionally obtained observations of the partial transits of 2018 February 18 and March 10 UT using the Multicolor Simultaneous Camera for studying Atmospheres of Transiting exoplanets 2 (MuSCAT2; Narita et al. 2018), which is also on the Telescopio Carlos Sánchez. MuSCAT2 observes simultaneously in the *g*, *r*, *i*, and *z* bands, using a set of dichroics to split the light between four separate cameras. The transit depth in all four MuSCAT2 bands for both partial transits is consistent with that from *K2*, giving no evidence for a chromatic transit depth and indicating that the inconsistent transit depths in the DEMONEXT data are indeed likely due to systematics and problems with the detrending. We also include the MuSCAT2 data in our simultaneous fits. We also show these data in Fig. 6.

The transit of K2-261 b is shallower than that of K2-260 b and not as easily detectable from the ground. We therefore did not obtain any follow-up transit photometry of K2-261 b.

2.4 High-resolution spectroscopy

After identification of the transiting planet candidates around K2-260 and K2-261, we obtained reconnaissance spectroscopy observations in order to measure the stellar parameters and rule out obvious false-positive scenarios (such as eclipsing binaries with two sets of strong lines). We obtained these spectra with the 2.7 m Harlan J. Smith Telescope at McDonald Observatory, Texas, USA, and its Robert G. Tull coudé spectrograph (Tull et al. 1995). We used the spectrograph in its TS23 configuration, which gives a spectral resolving power of $R = 60\,000$ over the range of 3750–10200 Å, with complete spectral coverage below 5691 Å. We obtained a spectrum of each K2-260 and K2-261 with a SNR per resolution element of 35 and 50 at 5650 Å for K2-260 and K2-261, respectively. We measured stellar parameters from these spectra using the Kea spectral analysis tool (Endl & Cochran 2016).

The reconnaissance spectra indicated that both K2-260 and K2-261 were good targets for precise radial velocity (RV) follow-up in order to confirm these planet candidates and measure their masses: both stars are relatively slowly rotating and have high-surface gravity, and neither of them show any evidence of multiple lines in the spectra. We obtained precise RVs with three different facilities; these have higher SNRs and so superseded the reconnaissance spectra in our further analyses.

We obtained observations of both K2-260 and K2-261 using the FIbre-fed Échelle Spectrograph (FIES; Frandsen & Lindberg 1999; Telting et al. 2014) on the 2.56 m Nordic Optical Telescope (NOT) at the Observatorio del Roque de los Muchachos, La Palma, Spain. We used FIES' *high-res* mode, which provides spectra with $R = 67\,000$ over the range of 3600–9000 Å. We used the same observing strategy as in Gandolfi et al. (2015); at each observation epoch, we obtained three consecutive exposures to facilitate cosmic ray removal, bracketed by 120–180-s ThAr exposures in order to trace any drift of the spectrograph. We obtained eighteen RVs of K2-260 with FIES between 2017 November 16 and 2018 March 11 UT, and twelve of K2-261 between 2017 December 26 and 2018 February 15 UT, as part of the observing programmes 56-010, 56-112, and 56-209.

We also obtained observations of both targets using the High Accuracy Radial velocity Planet Searcher for the Northern hemisphere (HARPS-N; Cosentino et al. 2012) spectrograph on the 3.58 m Telescopio Nazionale Galileo (TNG), also at La Palma. HARPS-N is a fibre-fed cross-dispersed échelle spectrograph, and provides spectra with $R = 115\,000$ over the range of 3830–6900 Å. We observed K2-261 nine times between 2017 December 27 and 2018 February 22 UT, and K2-260 twice on 2018 February 19 UT, as part of the programmes A36TAC_12, CAT17B_99, and OPT17B_059. We did not utilize the two HARPS-N RVs for K2-260 in our fits as their poor phase coverage results in little constraining power on the fits. Additionally, one HARPS-N RV of K2-261 was excluded from the fit due to poor SNR.

Finally, we obtained observations of K2-261 using the High Accuracy Radial velocity Planet Searcher (HARPS; Mayor et al. 2003). The spectrograph is essentially identical to HARPS-N, and is located on the ESO 3.6 m telescope at La Silla Observatory, Chile. We obtained 10 RV observations of K2-261 using HARPS between 2018 January 25 and May 13 UT under the programmes 0100.C.0808 and 0101.C-0829. One HARPS RV was excluded from our fits due to an incorrect flux correction by the HARPS pipeline.

For both HARPS and HARPS-N, we reduced the data using the dedicated off-line pipelines and extracted the RVs via cross-correlation with a G2 numerical mask (Baranne et al. 1996; Pepe et al. 2002). For FIES, we reduced the data as described in Gandolfi et al. (2015), using standard IRAF and IDL routines, which include bias subtraction, flat fielding, order tracing and extraction, and wavelength calibration. The FIES RVs of K2-260 were derived by cross-correlating the observed spectra against a high SNR (>300) spectrum of the RV standard star HD 50692 observed with the same instrument set-up as K2-260. For K2-261, relative RVs were extracted by cross-correlating the observed FIES data against the first stellar spectrum.

We show these data in Fig. 4, and list all of our RV measurements in Table 3, along with the cross-correlation function bisector span (BIS) and FWHM, and the Ca II H & K chromospheric activity index $\log R'_{\rm HK}$ (the latter measured only from the HARPS-N and HARPS spectra). We do not find any significant correlation between the RV measurements and the BIS, as well as between the RVs and the FWHMs, for either target, and we robustly detect the stellar RV variations induced by both transiting objects, confirming both K2-260 b and K2-261 b as bona fide planets.

3 ANALYSIS

3.1 Spectral analysis and stellar parameters

In order to derive more precise stellar parameters than were found using our reconnaissance spectra (Section 2.4), we analysed our co-added HARPS-N spectra of K2-261, and our co-added FIES spectra of K2-260. The spectroscopic analysis was performed within the ISPEC framework (Blanco-Cuaresma et al. 2014). We derived spectroscopic parameters ($T_{\rm eff}$, $\log g$, [Fe/H], $v_{\rm mic}$) by fitting synthetic spectra computed using MOOG (Sneden 1973) and ATLAS9 model atmospheres (Castelli & Kurucz 2004) to the co-added spectra. We computed the broadening function by convolving the observed spectrum with a sharp-lined template. The broadening function was fitted with a broadened line profile to obtain $v \sin i_\star$ and the macro-turbulent velocity $v_{\rm mac}$. For K2-260, we fixed the micro-turbulent velocity $v_{\rm mic}$ using the values from Doyle et al. (2014) expected based upon the $T_{\rm eff}$, $\log g_\star$, and [Fe/H] in the fit.

For K2-260, we could not obtain a good measurement of $\log g_\star$ from the spectra due to insufficient SNR and the moderate rotational broadening ($v \sin i_\star = 16.0 \pm 2.0$ km s^{-1}). We therefore estimated $\log g_\star = 4.15^{+0.02}_{-0.04}$ using the mean stellar density derived from the circular-orbit transit fit (Section 3.3) and BASTA isochrones (Silva Aguirre et al. 2015) with a flat prior over the range of 5500 K $< T_{\rm eff} <$ 7500 K. We fixed $\log g_\star$ to this value in the spectral analysis as the uncertainties are much smaller than generally obtainable from spectroscopy alone. For both stars, we leveraged the precise *Gaia* DR2 parallaxes (Gaia Collaboration et al. 2016, 2018) to fit the stellar SEDs, using the *BVgriJHK*-band photometry listed in Table 1. For K2-260, we included reddening of $E(B-V) = 0.18 \pm 0.006$ from Green et al. (2018), while for K2-261 we assumed $E(B-V) = 0$. The stellar parameters for the two stars are listed in Table 4.

We inferred the stellar masses, radii, and ages using the BASTA code to fit the measured $T_{\rm eff}$, [Fe/H], and mean stellar density to an isochrone grid from the BaSTI data base[2] computed using the FRANEC stellar evolutionary models (Pietrinferni et al. 2004). Our derived parameters are also listed in Table 4. Thanks to the location of both stars near the main-sequence turn-off we are able to measure relatively precise ages of 1.9 ± 0.3 Gyr for K2-260 and $8.8^{+0.4}_{-0.3}$ Gyr for K2-261. We show the position of both stars in the H–R diagram in Fig. 5.

We estimated spectral types for the stars based upon the $T_{\rm eff}$-spectral-type calibration of Pecaut & Mamajek (2013), obtaining spectral types of F6 and G7, respectively. K2-261 lies just past the main-sequence turn-off, and so we quote a spectral type of G7IV/V, while K2-260 lies at the main-sequence turn-off, resulting in a spectral type of F6V.

3.2 *UVW* space motion

We calculated the *UVW* space motion for both K2-260 and K2-261, since these stars have *Gaia* DR2 6-d kinematic measurements (i.e. position, parallax, proper motion, and RV; Gaia Collaboration et al. 2016, 2018). We used the IDL routine GAL_UVW,[3] which is based upon Johnson & Soderblom (1987). Using the local standard of rest (LSR) definition from Coşkunolu et al. (2011), we found that K2-260 has a space velocity of (U, V, W) = (15.8 ± 2.6, -6.15 ± 0.57, -9.46 ± 0.73) km s^{-1}, while K2-261 has (U, V, W) = (-8.99 ± 0.13, -29.14 ± 0.49, -21.81 ± 0.50) km s^{-1}, both in the LSR frame. We then used the methodology of Reddy, Lambert & Allende Prieto (2006) to estimate the probability that these stars belong to various Galactic components. We find that K2-260 has a 99 per cent probability of belonging to the Galactic thin disc, 1 per cent that it is a member of the thick disc, and 2×10^{-3} per cent that it belongs to the halo. This is expected as F stars are relatively young. K2-261 has a 97 per cent probability of belonging to the thin disc, 3 per cent that it is a member of the thick disc, and 8×10^{-3} per cent that it is a member of the halo. The high [Fe/H] of K2-261 found in Section 3.1 ([Fe/H] $= 0.36 \pm 0.06$) is also consistent with its membership in the Galactic thin disc.

3.3 Joint analysis of photometry and radial velocities

In order to measure the parameters of K2-260 b and K2-261 b, we simultaneously fit all of the available time-series photometry and RVs for each system. We use the same PYTHON-based fitting code used by Johnson et al. (2017), but modified to allow for non-zero orbital eccentricity. It samples the likelihood function of model fits to the data using an affine-invariant Markov chain Monte Carlo (MCMC) algorithm as implemented in EMCEE (Foreman-Mackey et al. 2013).

We generated photometric transit models using the BATMAN package (Kreidberg 2015). We assumed a quadratic limb darkening law and used the triangular sampling method of Kipping (2013) to uniformly sample the relevant parameter space. We calculated expected limb darkening values in each band using the JKTLD code (Southworth 2015) to interpolate limb darkening values to the best-fitting stellar $T_{\rm eff}$ and $\log g_\star$ measured earlier, from the tabulations provided for the *Kepler* bandpass by Sing (2010) and for the g, r, i, and z bands by Claret (2004).

For circular orbital fits, we simply modelled the RV curve as a cosine function, while for eccentric orbits we computed the RV model using the RADVEL package (Fulton et al. 2018, but note that we only used RADVEL to compute the model and did not use the fitting functions provided by that package). We fit for an individual RV offset γ for each facility, and also included an RV jitter term for each facility added in quadrature to the uncertainty on each RV data point.

All in all, our MCMCs included the following parameters: orbital period P, transit epoch T_0, radius ratio $R_P/R_\star$, impact parameter b, and the scaled semimajor axis $a/R_\star$; two quadratic limb-darkening parameters per photometric bandpass; the RV semiamplitude K and one RV offset γ and one RV jitter term per RV facility; for the fits

[2]The BaSTI database was developed by the Trieste Astronomical Observatory (INAF-OAT) and the Teramo Astronomical Observatory (INAF-OATeramo), and is maintained by S. Cassisi et al. It is available at http://ia2.oats.inaf.it/archives/basti-a-bag-for-stellar-tracks-and-isochrones

[3]https://idlastro.gsfc.nasa.gov/ftp/pro/astro/gal_uvw.pro

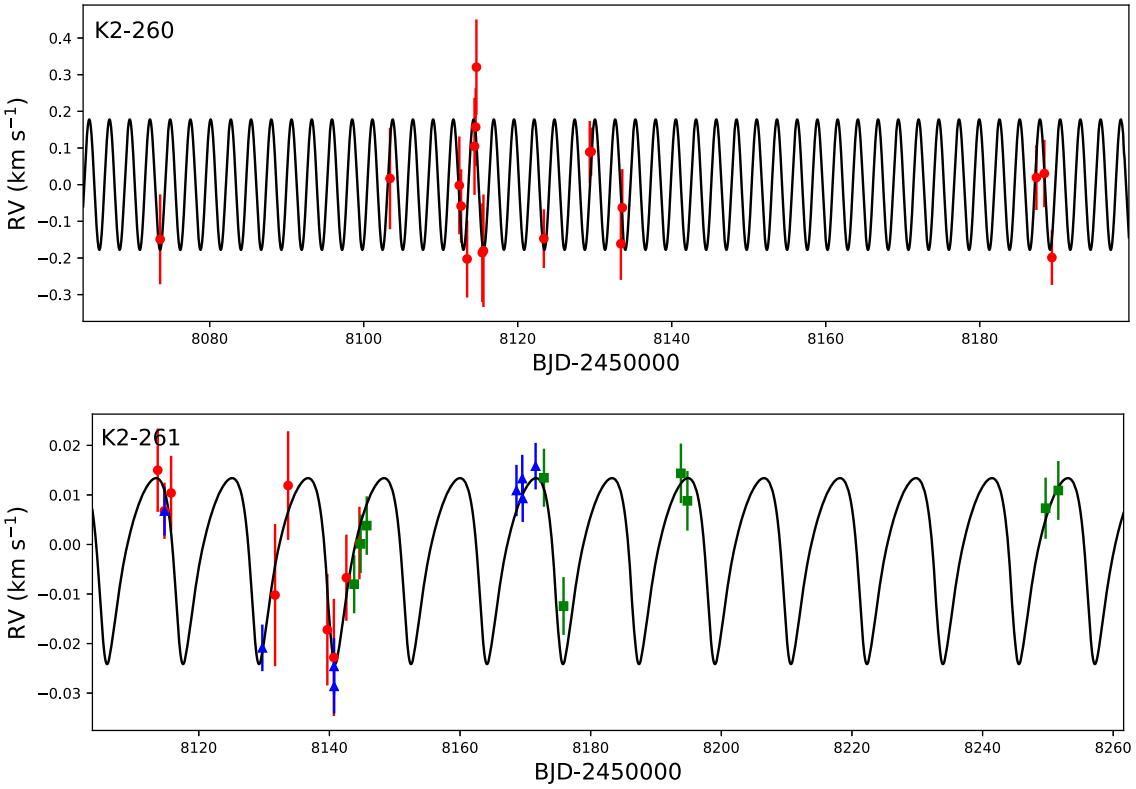

Figure 4. RV measurements of K2-260 (top) and K2-261 (bottom), along with the best-fitting orbit models computed in Section 3.3. Data from FIES are shown as circles (red in the online version), HARPS-N as triangles (blue online), and HARPS as squares (green online). The error bars incorporate both the internal RV errors and the best-fitting RV jitter.

including an RV trend, a linear acceleration term $\dot{\gamma}$; and, in the case of eccentric orbital fits, $e \sin \omega$ and $e \cos \omega$. We set Gaussian priors upon each limb darkening value with a σ-width of 0.1, and for the other parameters used uniform priors within physically allowed bounds, except as noted below. We performed fits with both circular and eccentric orbits for both planets, and we also performed fits including a linear RV trend for both systems in order to search for any evidence of RV trends due to additional objects in these systems.

3.3.1 K2-260

For K2-260, we do not find any evidence for an RV trend (i.e. $\dot{\gamma}$ is zero to within 1σ), and set 3σ limits of $-2.7 < \dot{\gamma} < 2.7$ m s^{-1} d^{-1}. Our final fits for K2-260 thus assumed $\dot{\gamma} = 0$. For the eccentric fit for K2-260 b, we set a Gaussian prior upon $e \cos \omega$ with a central value of -0.0049 and a width σ of 0.0048, based upon the best-fitting value of this parameter from the analysis of the secondary eclipse (Section 3.5).

We show the best-fitting light-curve and RV models for K2-260, along with the data, in Fig. 6. The best-fitting eccentricity from the eccentric model is non-zero at a significance of only 1.5σ, while $e \sin \omega$ is consistent with zero. Additionally, we separately measured that $e \cos \omega$ is also consistent with zero (Section 3.5). Finally, the Bayesian information criterion (BIC) shows a strong preference for the circular model, with $\Delta\mathrm{BIC} = 17.5$ in preference of the circular model. We therefore conclude that there is no compelling evidence that the orbit of K2-260 b is eccentric and adopt the circular fit. None the less, in the interests of completeness we list the best-fitting parameters from both fits in Table 5.

3.3.2 K2-261

We show the best-fitting light-curve model and *K2* data, and the RV curve for the eccentric orbital fit, for K2-261 in Fig. 7. For K2-261 b the eccentric fit prefers an eccentric orbit, with $e = 0.39 \pm 0.15$. While this is formally only a 2.6σ detection of a non-zero eccentricity, the BIC prefers the eccentric model, with a ΔBIC value of 9.3 in preference of the eccentric model. Since a ΔBIC value of <10 is not conclusive, we also conducted a more fully Bayesian model comparison. We computed the Bayes factor for the model comparison, using the marginal likelihood approximation of Chib & Jeliazkov (2001); we ported the implementation of this approximation from the BayesianTools R library (Hartig, Minunno & Paul 2017) to PYTHON for use with our MCMC chains. Doing so, we estimate a Bayes factor of 237 in preference of the eccentric model, indicating a decisive preference for the presence of orbital eccentricity for K2-261.

Including an RV trend results in a best-fitting value of $\dot{\gamma} = 0.106^{+0.051}_{-0.057}$ m s^{-1} d^{-1}, which is non-zero at the 2.1σ level and is thus marginally significant. This also improves the fit to the RV data. Including the trend, however, requires a more eccentric planetary orbit ($e = 0.52^{+0.12}_{-0.13}$), which results in a poorer fit to the *K2* light curve as the eccentricity affects the detailed light-curve shape. Furthermore, this requires an implausibly low mean stellar density of $0.032^{+0.061}_{-0.021}$ $\rho_\odot$, which is 3.3σ discrepant with the value expected from the spectroscopic stellar parameters (while the value from the

Table 3. RV measurements of K2-260 and K2-261.

BJD_{TDB}	RV ($km\,s^{-1}$)	σ_{RV} ($km\,s^{-1}$)	BIS ($km\,s^{-1}$)	FWHM ($km\,s^{-1}$)	$\log R'_{HK}$	$\sigma_{\log R'_{HK}}$	T_{exp} (s)	SNR	Instrument
K2-260									
2458073.56279	28.9213	0.1196	0.4946	28.3623	–	–	3600	23	FIES
2458103.41726	29.0872	0.1358	0.5607	28.0208	–	–	3600	25	FIES
2458112.41796	29.0684	0.1306	0.7535	28.5843	–	–	3600	21	FIES
2458112.64764	29.0119	0.0966	0.2418	28.1836	–	–	3600	28	FIES
2458113.42787	28.8675	0.1017	0.4048	28.2302	–	–	3600	28	FIES
2458114.38939	29.1748	0.1296	0.7658	28.3094	–	–	3600	20	FIES
2458114.54165	29.2274	0.1025	0.6633	28.4909	–	–	3600	24	FIES
2458114.63722	29.3908	0.1274	0.5007	28.2135	–	–	3600	18	FIES
2458115.40316	28.8845	0.1320	0.6163	28.4217	–	–	3600	21	FIES
2458115.55094	28.8900	0.1512	0.6702	28.1998	–	–	3600	14	FIES
2458123.39303	28.9230	0.0753	0.2370	28.1771	–	–	3600	29	FIES
2458129.35492	29.1592	0.0805	0.2508	29.0288	–	–	3600	27	FIES
2458129.53697	29.1604	0.0599	0.2017	28.1717	–	–	3600	26	FIES
2458133.39617	28.9090	0.0948	0.3268	28.5724	–	–	3600	28	FIES
2458133.57782	29.0075	0.1015	0.2893	28.2565	–	–	3600	26	FIES
2458187.35731	29.0897	0.0843	0.3350	29.2858	–	–	3600	25	FIES
2458188.38929	29.1007	0.0879	0.7315	28.1793	–	–	3600	26	FIES
2458189.36976	28.8715	0.0699	0.1347	28.8898	–	–	3600	24	FIES
2458169.40257	29.279	0.052	−1.206	26.5556	−4.594	0.062	3600	18	HARPS-N
2458169.44866	29.366	0.050	−6.231	27.0874	−4.674	0.071	3600	19	HARPS-N
K2-261									
2458113.71551	0.0000	0.0079	0.0005	12.4310	–	–	3600	52	FIES
2458114.74539	−0.0052	0.0049	0.0089	12.3931	–	–	3600	57	FIES
2458115.75979	−0.0045	0.0068	0.0065	12.4364	–	–	3600	63	FIES
2458131.68086	−0.0300	0.0140	0.0130	12.4362	–	–	3600	29	FIES
2458133.67474	−0.0068	0.0095	0.0081	12.4448	–	–	3600	38	FIES
2458139.68280	−0.0340	0.0110	0.0360	12.4553	–	–	3600	37	FIES
2458140.68126	−0.0350	0.0120	0.0130	12.3920	–	–	3600	38	FIES
2458142.59534	−0.0284	0.0084	0.0139	12.4582	–	–	3600	43	FIES
2458144.59629	−0.0115	0.0068	0.0082	12.3859	–	–	3600	44	FIES
2458146.69263	0.0020	0.0110	0.0200	12.4276	–	–	3600	35	FIES
2458163.53606	−0.0179	0.0056	0.0165	12.4710	–	–	3600	56	FIES
2458164.59738	−0.0369	0.0050	−0.0041	12.4503	–	–	3600	55	FIES
2458114.75801	3.3424	0.0019	−0.0058	7.4426	−5.139	0.043	900	43	HARPS-N
2458129.73171	3.3148	0.0011	−0.0087	7.4581	−5.129	0.019	1800	68	HARPS-N
2458140.70807	3.3110	0.0034	−0.0133	7.4584	−5.204	0.163	1200	29	HARPS-N
2458140.72396	3.3070	0.0030	0.0024	7.4599	−4.943	0.091	1200	33	HARPS-N
2458168.63918	3.3465	0.0025	−0.0006	7.4408	−5.169	0.066	2100	36	HARPS-N
2458169.52666	3.3489	0.0014	−0.0066	7.4393	−5.077	0.026	3300	55	HARPS-N
2458169.59477	3.3449	0.0013	−0.0069	7.4464	−5.056	0.021	3300	60	HARPS-N
2458169.70060[a]	3.2810[a]	0.0440[a]	−0.1753[a]	7.2957[a]	−4.545[a]	0.451[a]	267[a]	4†	HARPS-N[a]
2458171.56866	3.3514	0.0011	−0.0065	7.4418	−5.111	0.017	1500	70	HARPS-N
2458143.78984	3.3331	0.0013	−0.0093	7.4954	−5.177	0.031	1500	64	HARPS
2458144.77455	3.3412	0.0014	−0.0054	7.4928	−5.207	0.039	1200	58	HARPS
2458145.71595	3.3449	0.0014	−0.0050	7.4817	−5.208	0.040	1500	57	HARPS
2458171.71521[a]	3.3438[a]	0.0016[a]	−0.0179[a]	7.6649[a]	–	–	1500[a]	71[a]	HARPS[a]
2458172.84902	3.3546	0.0012	−0.0030	7.4881	−5.255	0.043	1500	67	HARPS
2458175.84594	3.3287	0.0011	−0.0056	7.4916	−5.184	0.035	1500	76	HARPS
2458193.81413	3.3555	0.0018	−0.0038	7.4958	−5.081	0.046	1200	46	HARPS
2458194.80916	3.3499	0.0018	0.0030	7.4968	−5.010	0.040	1200	47	HARPS
2458249.65186	3.3484	0.0023	0.0053	7.5094	−5.303	0.099	1200	37	HARPS
2458251.59291	3.3520	0.0016	−0.0014	7.4957	−5.194	0.048	1200	52	HARPS

Notes. We do not use the two HARPS-N spectra of K2-260 in our fits as the phase coverage is insufficient to provide good constraints upon the fits, and also excluded the two spectra marked as [a] from our fits due to low signal-to-noise and other problems. The FIES RVs of K2-261 are measured with respect to the first spectrum, the RV of which is arbitrarily set to zero. See Table 5 for the best-fitting RV offsets for each dataset. We did not measure the activity index $\log R'_{HK}$ from our FIES spectra as our pipeline is not configured to do so. The bisector spans quoted for the HARPS-N data on K2-260 are likely inaccurate as they were derived using the pipeline G2 CCF mask, which is not a good match to the F6 spectral type of the target. The quoted signal-to-noise ratio (SNR) is the per-pixel SNR measured at 5500 Å.

Table 4. Stellar parameters of K2-260 and K2-261.

Parameter	K2-260	K2-261
Measured parameters		
$T_{\rm eff}$ (K)	6367 ± 250	5537 ± 71
$\log g_\star$(cgs)	4.15 (fixed)	4.21 ± 0.11
[Fe/H] (dex)	-0.14 ± 0.15	0.36 ± 0.06
$v \sin i_\star$ ($\rm km\,s^{-1}$)	16.0 ± 2.0	2.8 ± 0.5
$v_{\rm mic}$ ($\rm km\,s^{-1}$)	1.6 (fixed)	1.3 ± 0.1
$v_{\rm mac}$ ($\rm km\,s^{-1}$)	10.0 ± 2.0	2.2 ± 0.5
Derived parameters		
Spec. type	F6V	G7IV/V
$M_\star$ ($\rm M_\odot$)	$1.39^{+0.05}_{-0.06}$	$1.10^{+0.01}_{-0.02}$
$R_\star$ ($\rm R_\odot$)	1.69 ± 0.03	1.65 ± 0.04
$\rho_\star$ ($\rho_\odot$)	0.2841 ± 0.0071	0.248 ± 0.021
age (Gyr)	1.9 ± 0.3	$8.8^{+0.4}_{-0.3}$

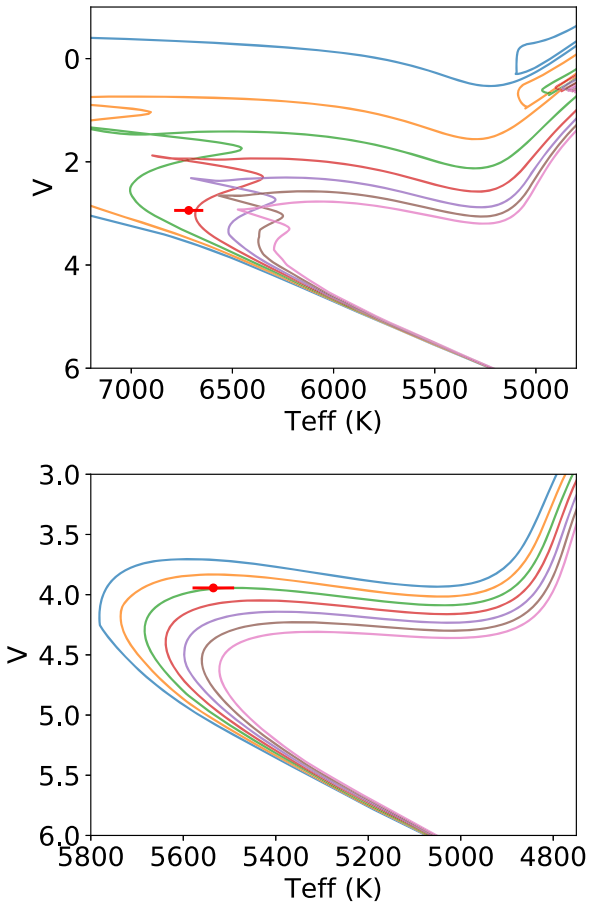

Figure 5. H–R diagrams showing K2-260 (top) and K2-261 (bottom). For K2-260 the lines show BaSTI isochrones of, from top to bottom, 0.5 (coloured blue online), 1.0 (orange), 1.5 (green), 2.0 (red), 2.5 (purple), 3.0 (brown), and 3.5 (pink) Gyr for [Fe/H] = −0.1, while for K2-261 the lines show isochrones with ages of, from left to right, 7 (blue), 8 (orange), 9 (green), 10 (red), 11 (purple), 12 (brown), and 13 (pink) Gyr for [Fe/H] = +0.4. Coincidentally, both K2-260 and K2-261 are located near the main-sequence turn-off, although K2-261 has already passed this point whereas K2-260 is only now reaching it.

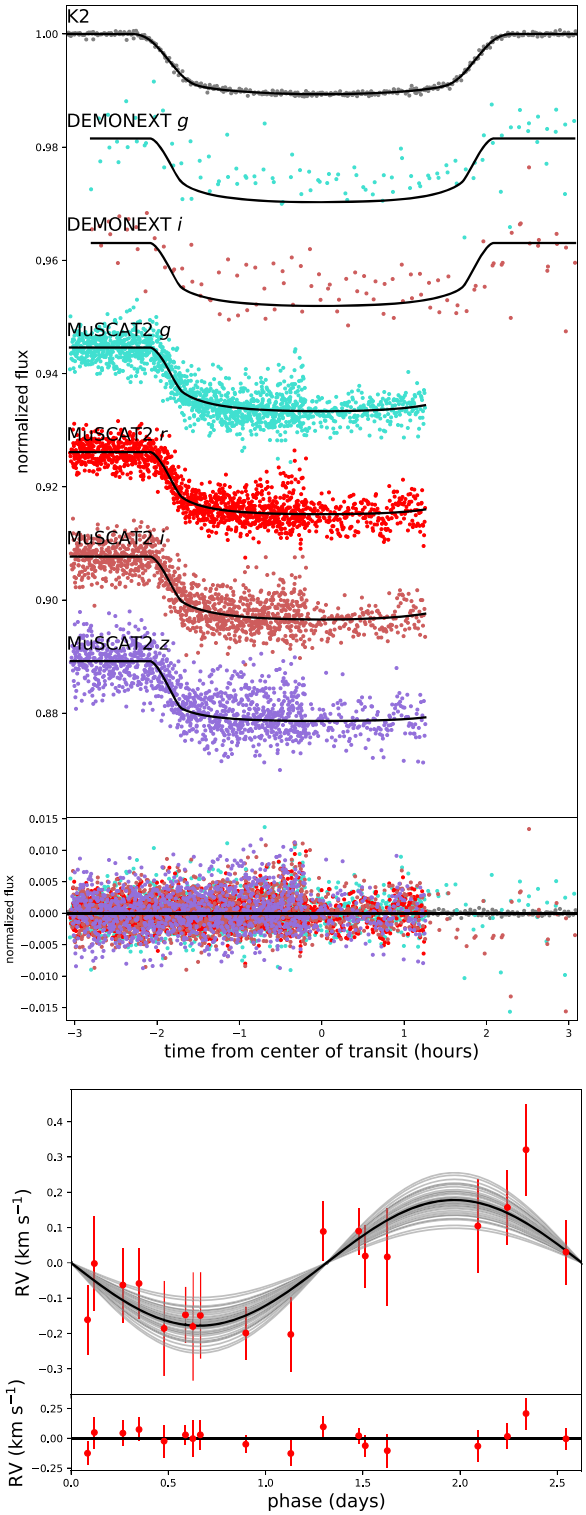

Figure 6. Top: light curves of K2-260, phase-folded on the transit period and with the best-fitting transit models overplotted. The transits in each band-instrument combination are offset vertically by an arbitrary amount for clarity; note that both the DEMONEXT and MuSCAT2 light curves contain two individual transits overplotted. Bottom: RV measurements for K2-260 phased to the transit period, with the best-fitting model from the circular orbital fit overplotted in black. The RV curves corresponding to 50 random draws from the posterior distributions are overplotted in grey. The error bars incorporate both the internal RV errors and the best-fitting RV jitter.

Table 5. Planetary parameters of K2-260 b and K2-261 b.

Parameter (unit)	K2-260 b circular fit (preferred)	K2-260 b eccentric fit	K2-261 b circular fit	K2-261 b eccentric fit (preferred)
ΔBIC (circular − eccentric)	−17.5		9.3	
MCMC parameters				
P (d)	2.6266657 ± 0.0000018	$2.6266657^{+0.0000020}_{-0.0000018}$	11.63344 ± 0.00012	11.63344 ± 0.00012
T_0 (BJD)	$2457820.738135 \pm 0.000090$	$2457820.738133^{+0.000091}_{-0.000098}$	$2457906.84115 \pm 0.00045$	$2457906.84084^{+0.00054}_{-0.00067}$
$R_P/R_\star$	$0.09731^{+0.00032}_{-0.00025}$	$0.09731^{+0.00033}_{-0.00027}$	$0.05281^{+0.00104}_{-0.00051}$	$0.05293^{+0.00096}_{-0.00051}$
$a/R_\star$	$5.291^{+0.033}_{-0.073}$	$5.34^{+0.92}_{-1.00}$	$17.79^{+0.57}_{-1.00}$	$13.3^{+2.4}_{-2.6}$
b	$0.122^{+0.090}_{-0.082}$	$0.116^{+0.096}_{-0.083}$	$0.27^{+0.19}_{-0.18}$	0.27 ± 0.18
$e \sin\omega$	0 (fixed)	$-0.02^{+0.21}_{-0.17}$	0 (fixed)	$0.22^{+0.16}_{-0.13}$
$e \cos\omega$	0 (fixed)	$-0.0025^{+0.0042}_{-0.0040}$	0 (fixed)	$-0.29^{+0.12}_{-0.11}$
K (km s^{-1})	$0.178^{+0.038}_{-0.039}$	$0.174^{+0.040}_{-0.041}$	$0.0137^{+0.0023}_{-0.0021}$	0.0188 ± 0.0026
$\gamma_{\rm FIES}$ (km s^{-1})	29.070 ± 0.025	$29.067^{+0.026}_{-0.027}$	-0.0137 ± 0.0032	$-0.0147^{+0.0032}_{-0.0031}$
$\gamma_{\rm HARPS\text{-}N}$ (km s^{-1})			3.3323 ± 0.0044	$3.3356^{+0.0018}_{-0.0024}$
$\gamma_{\rm HARPS}$ (km s^{-1})			3.3428 ± 0.0017	$3.3411^{+0.0021}_{-0.0023}$
jitter$_{\rm FIES}$ (km s^{-1})	$0.027^{+0.030}_{-0.019}$	$0.028^{+0.029}_{-0.019}$	$0.0042^{+0.0047}_{-0.0029}$	$0.0032^{+0.0037}_{-0.0022}$
jitter$_{\rm HARPS\text{-}N}$ (km s^{-1})			$0.0121^{+0.0054}_{-0.0033}$	$0.0046^{+0.0034}_{-0.0021}$
jitter$_{\rm HARPS}$ (km s^{-1})			$0.0045^{+0.0020}_{-0.0013}$	$0.0057^{+0.0027}_{-0.0019}$
Derived parameters				
δ (per cent)	$0.9470^{+0.0062}_{-0.0048}$	$0.9470^{+0.0064}_{-0.0053}$	$0.2789^{+0.0111}_{-0.0054}$	$0.2801^{+0.0102}_{-0.0054}$
i (°)	$88.67^{+0.89}_{-1.00}$	$88.76^{+0.86}_{-1.00}$	$89.15^{+0.58}_{-0.75}$	$88.4^{+1.1}_{-1.9}$
$\rho_\star$ ($\rho_\odot$)	$0.2881^{+0.0054}_{-0.0100}$	$0.33^{+0.60}_{-0.23}$	$0.558^{+0.055}_{-0.100}$	$0.100^{+0.160}_{-0.073}$
T_{14} (d)	$0.17365^{+0.00045}_{-0.00040}$	$0.171^{+0.041}_{-0.026}$	$0.2124^{+0.0018}_{-0.0014}$	$0.213^{+0.057}_{-0.029}$
T_{23} (d)	$0.14196^{+0.00049}_{-0.00073}$	$0.140^{+0.033}_{-0.021}$	$0.1891^{+0.0015}_{-0.0027}$	$0.189^{+0.051}_{-0.025}$
$T_{\rm peri}$ (BJD)	$2457820.738135 \pm 0.000090$	$2457820.757^{+1.281}_{-0.050}$	$2457906.84115 \pm 0.00045$	$2457907.58^{+0.59}_{-0.40}$
e	0 (fixed)	$0.134^{+0.124}_{-0.092}$	0 (fixed)	0.39 ± 0.15
ω (°)	90 (fixed)	$262.0^{+7.9}_{-170.0}$	90 (fixed)	143.0 ± 18.0
a (au)	$0.0404^{+0.0013}_{-0.0016}$	$0.0407^{+0.0071}_{-0.0078}$	$0.1365^{+0.0055}_{-0.0100}$	$0.102^{+0.019}_{-0.020}$
R_P (R_J)	$1.552^{+0.048}_{-0.057}$	$1.552^{+0.048}_{-0.057}$	$0.848^{+0.026}_{-0.022}$	$0.850^{+0.026}_{-0.022}$
M_P (M_J)	$1.42^{+0.31}_{-0.32}$	$1.39^{+0.32}_{-0.34}$	$0.163^{+0.028}_{-0.025}$	0.223 ± 0.031
$M_P \sin i$ (M_J)	$1.42^{+0.31}_{-0.32}$	$1.39^{+0.32}_{-0.34}$	$0.163^{+0.028}_{-0.025}$	0.223 ± 0.031
$M_P/M_\star$	0.00107 ± 0.00025	$0.00104^{+0.00026}_{-0.00027}$	$0.000141^{+0.000024}_{-0.000022}$	0.000194 ± 0.000027
log g_P (cgs)	$3.164^{+0.091}_{-0.100}$	$3.154^{+0.095}_{-0.100}$	$2.750^{+0.071}_{-0.079}$	$2.884^{+0.059}_{-0.072}$
ρ_P (g cm^{-3})	0.50 ± 0.12	0.49 ± 0.13	$0.355^{+0.067}_{-0.064}$	$0.483^{+0.076}_{-0.081}$
$T_{\rm eq}$ (K)	1957^{+78}_{-77}	1950^{+200}_{-190}	928^{+37}_{-19}	1080^{+110}_{-100}
H (km)	550 ± 130	560 ± 150	680 ± 120	580^{+110}_{-100}
$2H/R_P$	0.0102 ± 0.0024	$0.0104^{+0.0028}_{-0.0027}$	$0.0230^{+0.0040}_{-0.0042}$	$0.0195^{+0.0036}_{-0.0034}$

Notes. In the case of circular orbits the epoch of periastron $T_{\rm peri}$ is identical to the transit epoch as we fix $\omega = 90°$. The atmospheric scale height H assumes a hydrogen-dominated atmosphere (i.e. a mean molecular weight of 2), and the quantity $2H/R_P$ is the fractional surface area of the planetary disc subtended by an atmosphere of thickness H.

eccentric fit with no trend is only 0.9σ from this expected value, and the circular fit is 3.0σ away). While the model including the trend is disfavoured by only ΔBIC $= 0.3$ with respect to the eccentric model, we disfavour this model based upon the implausibly low $\rho_\star$ and we conclude that the inclusion of an RV slope results in a physically disallowed solution. For the above reasons, we therefore adopt the eccentric fit with no RV trend as our preferred solution for K2-261; most of the planetary parameters are consistent between the circular and eccentric fits, although the RV semi-amplitude K and thus the planetary mass is slightly smaller for the circular fit. We list the parameters from both of these fits with $\dot{\gamma}$ fixed to zero in Table 5.

3.4 Stellar rotation and inclination

Stellar variability with a quasi-sinusoidal shape is easily visible in the *K2* light curve of K2-260 (Fig. 1). The period of the variations, approximately 2 d, is too long to be due to δ Sct pulsations, and γ Dor pulsators tend to be hotter than K2-260 (see e.g. Uytterhoeven et al. 2011). This may therefore be rotational variability. We performed a Fourier analysis of the light curve, finding that the most dominant frequency is at 0.462 cycles day^{-1} ($P = 2.16$ d); the first harmonic at 0.92 cycles day^{-1} ($P = 1.08$ d) is also present. This frequency structure is what would be expected for rotation with a period near 2 d; pulsations would result in a different frequency

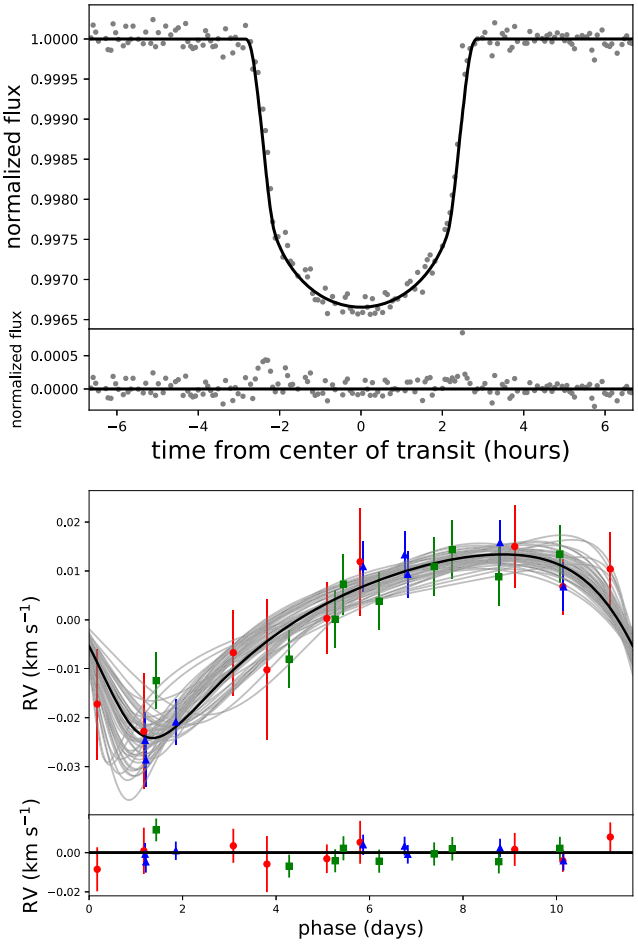

Figure 7. Top: *K2* light curve of K2-261, phase-folded on the transit period and with the best-fitting transit model overplotted. Bottom: RV measurements of K2-261 from FIES (circles, coloured red online), HARPS-N (triangles, blue online), and HARPS (squares, green online), phased to the transit period and with the best-fitting RV model overplotted in black, along with the models corresponding to 50 random draws from the posterior distributions in grey. The error bars incorporate both the internal RV errors and the best-fitting RV jitter.

structure. We cannot, however, exclude the possibility that the 2-d peak could in fact be a harmonic and that the actual rotation period could be an integer multiple of this. We will discuss this possibility in more detail below. There are also several strong peaks with periods of ten to several tens of days, which could be due to evolution of the spot pattern, but a detailed frequency analysis is beyond the scope of this paper.

We measured the details of the 2-d peak using two different methodologies: a Lomb–Scargle periodogram analysis (Lomb 1976; Scargle 1982; Zechmeister & Kürster 2009), and an autocorrelation function analysis (McQuillan, Mazeh & Aigrain 2014). In both cases, we estimated the uncertainty on the period using the FWHM of the relevant peak. From the periodogram analysis, we found a period of 2.169 ± 0.048 d and from the autocorrelation function 2.16 ± 0.49 d. Both values are consistent but we conservatively adopt the less-certain autocorrelation value.

As mentioned above, while the 2.16-d period may be the rotation period of K2-260, we cannot exclude the possibility that the rotation period may in fact be an integer multiple of this value. In Table 6, we list the rotation period, expected equatorial rotation velocity, implied value of $\sin i_\star$, and 1σ allowed range of $i_\star$ assuming that the true rotation period is 1, 2, 3, or 4 times the 2.16-d period from the light curve.

Table 6. Possible rotation periods of K2-260 and consequences thereof.

	$P_{\rm rot}$ (days)	$v_{\rm eq}$ ($\rm km\,s^{-1}$)	$\sin i_\star$	1σ range $i_\star$ (°)
1	2.16 ± 0.49	39.6 ± 9.0	0.40 ± 0.10	17.4–30.6
2	4.32 ± 0.98	19.8 ± 4.5	0.81 ± 0.21	>36.8
3	6.5 ± 1.5	13.2 ± 3.0	1.22 ± 0.32	>63.7
4	8.6 ± 2.0	9.9 ± 2.3	1.61 ± 0.43	None

Several points of interest are revealed by this analysis. First, if the rotation period is in fact 2.16 d, the predicted equatorial rotational velocity is 39.6 ± 9.0 $\rm km\,s^{-1}$, more than twice the measured $v \sin i_\star$ of 16.0 ± 2.0 $\rm km\,s^{-1}$. This would require that the rotation axis of K2-260 be significantly inclined with respect to the plane of the sky: $i_\star = 23.8^{+6.7}_{-6.4}$°. An equatorial velocity of 40 $\rm km\,s^{-1}$, however, is much higher than typical for stars with the spectral type of K2-260; stars with $T_{\rm eff} \sim 6350$ K typically have $v \sin i_\star < 20$ $\rm km\,s^{-1}$ (see e.g. fig. 4 of Winn et al. 2017). This suggests that it is *a priori* unlikely that the rotation period of K2-260 is in fact 2.16 d, but this cannot be excluded on the basis of our current data.

If the rotation period of K2-260 is in fact two or three times this (4.32 or 6.5 d), then the expected equatorial velocities are 19.8 ± 4.5 or 13.2 ± 3.0 $\rm km\,s^{-1}$, respectively, both of which are consistent to within 1σ with the measured $v \sin i_\star$, and are also well within the range of $v \sin i_\star$ values expected for a star of the spectral type of K2-260. On the other hand, in order to explain the quasi-sinusoidal shape of the light curve on a 2.16-d period with a longer rotation period, the spot distribution on the surface of K2-260 would need to have a near-symmetrical two- or three-spot configuration. In these cases, a large inclination of the stellar rotation axis is not required. Indeed, we are only able to set loose 1σ constraints of $i_\star > 36.8$° and >63.7° for these two cases. For the 6.5-d rotation period case, we note that this requires $\sin i_\star > 1$ (we find $\sin i_\star = 1.22 \pm 0.32$), but this is still consistent with 1 to within 1σ. A rotation period of 4 times 2.16 d or greater would require a value of $\sin i_\star$ increasingly larger than 1, excluding such values. These would also require increasingly complex and near-symmetrical multipolar distributions of spots, which are unlikely.

We therefore conclude that the rotation period of K2-260 is one of 2.16, 4.32, or 6.5 d, but cannot confidently distinguish among these possibilities. We will discuss the implications of these possible rotation periods in more detail in Section 4.3.

Although sufficient spot coverage to induce measurable rotational modulation is unusual for late F stars, it is not unprecedented; for instance, Mazeh et al. (2015) were able to measure rotation periods for numerous stars in the *Kepler* field with $T_{\rm eff}$ values as high as 6500 K.

We did not detect any significant rotational modulation in the light curve of K2-261, and so we cannot perform a similar analysis for that star. Based upon our values of $v \sin i_\star$ and $R_\star$ for this object, we calculate a 1σ upper limit on the expected rotation period of 37.2 d. The more pole-on K2-261 is viewed, the shorter the rotation period must be to explain the measured $v \sin i_\star$.

3.5 Secondary eclipse of K2-260

We searched the *K2* light curve for a secondary eclipse for K2-260, which, if of large enough magnitude, could have indicated that the

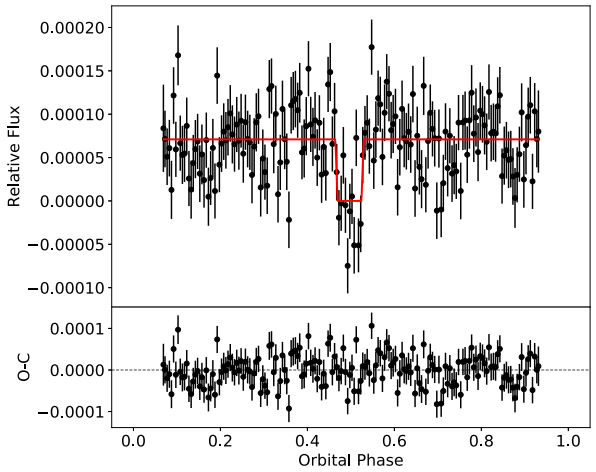

Figure 8. *K2* light curve of K2-260 (top), after the stellar variability and in-transit data have been removed and the data have been folded and binned on the orbital period. We show the data in black, and the best-fitting secondary eclipse model as a dashed line (solid red online). The residuals to the fit are shown in the bottom panel.

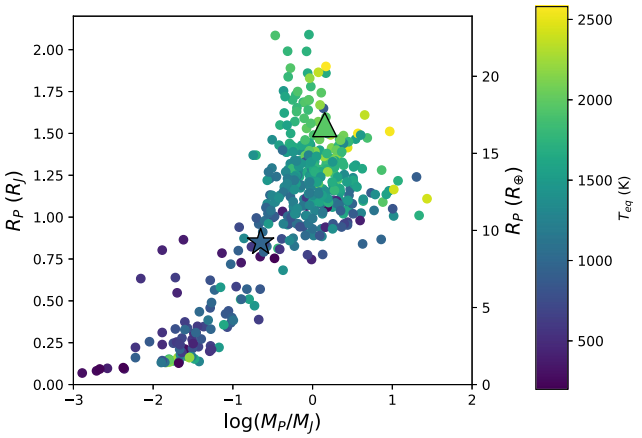

Figure 9. K2-260 b (triangle) and K2-261 b (star) in context with the population of transiting planets with mass and radius measurements, as obtained from the NASA Exoplanet Archive (compiled bythe NASA Exoplanet Science Institute and available at https://exoplanetarchive.ipac.caltech.edu/) on 2018 March 7. The plot points are coloured according to the zero-albedo equilibrium temperature T_{eq}.

system was a false positive. We subtracted the stellar variability of K2-260 by fitting a second-order polynomial to each $0.25\times$ P_{orb} portion of the out-of-transit light curve. This aggressive detrending procedure was necessitated by the stellar variability with a period close to the planetary orbital period (2.16 d versus 2.63 d; see Section 3.4). Although this detrending should have also removed any phase curve that might be present in the *K2* light curve, disentangling the phase curve and stellar variability will be very difficult (see Section 4.4 for further discussion), and so we chose to detrend out both the stellar variability and the phase curve and concentrate on detecting the secondary eclipse. We phase-folded and binned the detrended *K2* light curve on the planetary orbital period, which is shown in Fig. 8. We do indeed detect a secondary eclipse.

We fit the eclipse with an occultation model and an MCMC procedure. We obtain a best-fitting secondary eclipse depth of $\delta_{sec} = 71 \pm 15$ ppm, as well as $e\cos\omega = -0.0049^{+0.0048}_{-0.0036}$. The secondary eclipse depth is small and is consistent with K2-260 b being a planet (which is also confirmed by our RV measurements). See Section 4.4 for further discussion.

The value of $e\cos\omega$ that we obtained is consistent with zero to within 1.4σ. We thus conclude that there is no compelling evidence from the secondary eclipse for any orbital eccentricity, nor is there from the RV data (Section 3.3).

4 DISCUSSION

4.1 Properties of the planets and systems

In many ways, both K2-260 b and K2-261 b are typical representatives of the populations to which they belong. In Fig. 9, we show these two planets in context in the mass–radius diagram.

K2-260 b is a fairly typical hot Jupiter of 1.4 M_J and 1.6 R_J on a circular 2.6-d orbit. It is slightly inflated, which is expected for its mass and zero-albedo equilibrium temperature of ∼2000 K; planets in this region of the mass–radius diagram tend to have similar equilibrium temperatures (Fig. 9). K2-260 b is most noteworthy in that there is a possibility that its orbit may be misaligned with respect to its host star's rotation (Section 4.3) and that it shows a secondary eclipse in the *Kepler* bandpass (Section 4.4).

K2-261 b is also exemplary of the population of warm Saturns. Although its radius is somewhat too large to be part of the population of sub-Saturns identified by Petigura et al. (2017) – its radius is 9.2 $R_\oplus$, while Petigura et al. (2017) defined sub-Saturns as having radii between 4 and 8 $R_\oplus$– it none the less follows many of the same trends seen in this population. For instance, like warm sub-Saturns around metal-rich stars (Petigura et al. 2017), K2-261 b has an eccentric orbit, no additional known planets in the system, and a relatively high mass (65 $M_\oplus$, which is at the upper end of the range typical of sub-Saturns).

K2-261 is also interesting in that it is one of the older planet-host stars with a well-determined age. The NASA Exoplanet Archive[4] lists only 18 planet-host stars (as of 2017 May 24) with ages of >8.5 Gyr and an age uncertainty of less than 2 Gyr. K2-261 is among the most metal rich of these systems, although its metallicity is not unprecedented for a star of this age (cf. fig. 10 of Silva Aguirre et al. 2018).

K2-261 b is additionally one of three recently discovered $P \sim$ 12-d warm Saturns on eccentric orbits around bright stars from *K2*, along with K2-232 b (Brahm et al. 2018b; Yu et al. 2018) and K2-234 b (Van Eylen et al. 2018; Yu et al. 2018). Although K2-261 b is somewhat fainter than either of these stars (which have $V = 9.3$ and $V = 9.9$, respectively), it is none the less bright enough to enable many follow-up observations, and will allow comparisons to these other planets. It is intermediate in mass and radius to these two, and the system also has a very similar age to K2-234 (Van Eylen et al. 2018), which will also be helpful for comparative planetology.

4.2 Candidate stellar companion to K2-260

As discussed in Section 2.2, we detected a candidate stellar companion to K2-260 using our Subaru IRCS high-resolution imaging. As can be seen in Fig. 2, the candidate companion is close to the speckle pattern, but we found that it has a contrast of more than 5σ and is therefore likely to be real.

As we only have a single epoch of single-band imaging, we cannot confirm the association of the candidate companion via the

[4]https://exoplanetarchive.ipac.caltech.edu/

usual methods of common proper motion or colours, indicating that it is consistent with being located at the same distance. We therefore must rely upon probabilistic arguments. In order to assess the probability that the candidate companion is indeed physically associated with K2-260, we followed essentially the same methodology as used by Johnson et al. (2018) to estimate the probability that the candidate companion could be a background source. We obtained Galactic models computed by the TRILEGAL[5] (Girardi et al. 2005) and BESANÇON[6] (Robin et al. 2003) codes for the coordinates of K2-260. We used the default parameters for both codes, except for using the Schlafly & Finkbeiner (2011) reddening maps[7] for TRILEGAL and the Marshall et al. (2006) dust map for BESANÇON. We then counted the number of sources in each model, and used this to estimate the probability that there would be a background source at least as bright as the candidate companion at least as close to K2-260 as the candidate companion. We found that the probability of such a chance superposition is 0.13 per cent for the TRILEGAL model, and 0.016 per cent for the BESANÇON model. Although these estimates are in disagreement with each other by about an order of magnitude, we none the less conclude that the candidate companion is very likely to be physically associated with the K2-260 system. We caution, however, that we cannot confirm its association with our current data. We proceed for the remainder of the section with further analyses under the assumption that the candidate companion is indeed physically bound to K2-260.

We used the ISOCHRONES package (Morton et al. 2016) to estimate what stellar properties of the candidate companion would result in the observed ΔH value, given the properties of the primary. Using the 2MASS H-band magnitude and *Gaia* DR2 parallax, K2-260 has an absolute magnitude of $M_H = 2.039 \pm 0.069$, and the candidate companion therefore has $M_H = 8.78 \pm 0.19$. This corresponds to a mass of $\sim$0.13–0.16 $M_\odot$ for the candidate companion, taking into account the uncertainties on the age and metallicity of the primary. This would correspond to $T_{\rm eff} \sim$ 3200–3300 K, or, per Kraus & Hillenbrand (2007), a spectral type of M5-6V.

The candidate companion is too faint to significantly affect our other analyses of this system. Assuming the stellar parameters found earlier, the companion would have a magnitude ratio in the *Kepler* bandpass of $\Delta Kp \sim 9.5$ (again using ISOCHRONES). This would result in a dilution of the transit depth of K2-260 of less than two parts in 10^{-5}, which is much smaller than the uncertainty on the transit depth due to the photometric noise in the light curve, and is thus negligible. Similarly, the companion is too faint to be an eclipsing binary causing the transits of K2-260; in order to cause a transit of the observed depth, even a 100 per cent deep eclipse would need to occur on a companion no fainter than $\Delta Kp \sim 5.1$. This possibility is also excluded by our detection of the reflex motion of K2-260 due to the planet, and the achromaticity of the transit in our MuSCAT2 data.

The discovery of a candidate stellar companion to K2-260 is scientifically interesting for a number of reasons. Ngo et al. (2016) found that host stars of hot Jupiters are significantly more likely than field stars to host stellar companions between 50 and 2000 au, which tend to have mass ratios smaller than would be expected given the population of field binaries. The candidate companion to K2-260 fits this trend, with its projected separation of 400 au and mass ratio of $\sim$0.1, and is furthermore close and massive enough to likely be able to drive planetary migration via Kozai–Lidov oscillations (e.g. Fabrycky & Tremaine 2007; Naoz, Farr & Rasio 2012). We therefore encourage additional observations of K2-260 to confirm whether the candidate companion is bound to the system.

[5] http://stev.oapd.inaf.it/cgi-bin/trilegal_1.6
[6] http://model2016.obs-besancon.fr/
[7] https://irsa.ipac.caltech.edu/applications/DUST/

4.3 Orbital alignment of K2-260 b

Based upon the rotational variability in the light curve of K2-260 (Section 3.4), we found that the rotation axis of K2-260 may be significantly inclined with respect to the plane of the sky, depending upon whether the true rotation period is 2.16 d or an integer multiple thereof. This has consequences for the orbit of the planet. If the stellar rotation axis is inclined with respect to the plane of the sky, then the planetary orbit must have a substantial obliquity with respect to the stellar spin in order to transit. This would not be unexpected, as K2-260 is above the Kraft break (Kraft 1967), the point on the main sequence above which stars rotate rapidly due to their lack of a deep surface convective zone, a strong magnetic dynamo, and consequent rotational braking. Hot Jupiters around stars above the Kraft break often have substantially misaligned orbits (Winn et al. 2010; Albrecht et al. 2012). If instead the rotation period is twice or three times 2.16 d, a large stellar inclination, and therefore a misaligned orbit, are not required. This does not, however, exclude the possibility of a misaligned orbit; even if the stellar rotation axis is perpendicular to the line of sight, the sky-projected spin-orbit misalignment λ can be large. We cannot constrain λ with our current data, but this could easily be measured using the Rossiter–McLaughlin effect (Section 4.5).

We also note that if the rotation period is in fact 2.16 d, this is close to the 2.63-d planetary orbital period. Systems with $P_{\rm orb} \sim P_{\rm rot}$ have different tidal dynamics from those with rotation periods much different from the orbital period, including likely enhanced tidal dissipation (e.g. Collier Cameron & Jardine 2018), and therefore K2-260 may be of interest from this standpoint. As also discussed by Collier Cameron & Jardine (2018), the dissipation is likely different for spin-orbit misaligned systems near the stellar rotation period due to the different motion of the tidal bulge, providing additional motivation to measure the Rossiter–McLaughlin effect for K2-260 (Section 4.5). In addition, K2-260 may join a number of F stars with hot Jupiters, where the stellar rotation is quasi-synchronized to the planetary orbit, such as τ Boo (Donati et al. 2008) and CoRoT-4 (Lanza et al. 2009). Such systems were predicted to be an effective end point of hot Jupiter tidal evolution for F stars by Damiani & Lanza (2015), as reduced tidal damping when $P_{\rm rot} \sim P_{\rm orb}$ will delay the planet reaching the point where it can be tidally disrupted. K2-260's relatively advanced age for an F star, near the main-sequence turn-off, is consistent with this picture; the system has had ample time to evolve into such a quais-stable state. On the other hand, Collier Cameron & Jardine (2018) found evidence of *stronger* tidal damping for (aligned) systems with $P_{\rm rot} \sim P_{\rm orb}$. K2-260 could thus offer an opportunity to test the impact of any spin-orbit misalignment upon this evolution.

4.4 Secondary eclipse of K2-260 b

K2-260 b is one of a relatively small number of planets with a significantly detected secondary eclipse in the *Kepler* bandpass, and the first such hot Jupiter discovered using *K2* (although K2-113 b has a 1.9σ detection of the secondary eclipse, and the ultra short period planet K2-141 b also has a detected secondary eclipse: Espinoza et al. 2017; Malavolta et al. 2018).

From Esteves, De Mooij & Jayawardhana (2013), the secondary eclipse depth in the *Kepler* bandpass is

$$\delta_{\rm sec} = \left(\frac{R_P}{R_\star}\right)^2 \frac{\int B_\lambda(T_{\rm B}) T_K \, {\rm d}\lambda}{\int F_\lambda T_{\rm K} \, {\rm d}\lambda} + A_{\rm g}\left(\frac{R_P}{R_\star}\frac{R_\star}{a}\right)^2, \quad (1)$$

where B_λ is the Planck function, $T_{\rm B}$ is the blackbody temperature of the planetary dayside, $T_{\rm K}$ is the *Kepler* bandpass transmission function, F_λ is the stellar flux, and $A_{\rm g}$ is the planetary geometric albedo. This is equation 18 of Esteves et al. (2013), slightly rewritten to accommodate the notation and measured quantities in this article. The first term on the right-hand side of equation (1) describes the thermal emission in the *Kepler* bandpass, while the second term is the contribution of reflected starlight.

We numerically solve this equation for the geometric albedo $A_{\rm g}$, assuming, after Esteves et al. (2013), that $T_{\rm B} = T_{\rm eq}(A_{\rm B})$, where $A_{\rm B} = 3/2A_{\rm g}$ is the Bond albedo, and $T_{\rm eq} = T_{\rm eff}\sqrt{f R_\star/a}(1 - A_{\rm B})^2$, where f describes the efficiency of heat redistribution. We used two different limiting cases: homogeneous re-distribution of heat ($f = 1/4$) and instant re-radiation from the dayside ($f = 2/3$). We also make the simplifying assumptions that the planetary emission and stellar flux are both blackbodies, and that the *Kepler* bandpass is a tophat function between 4000 and 9000 Å (following Huber, Czesla & Schmitt 2017). In both heat redistribution cases, the eclipse depth requires a geometric albedo of $A_{\rm g} \sim 0.2$, and the contribution of thermal emission in the *Kepler* bandpass is small. Although this estimate is not likely to be completely accurate due to the approximations that we have made, it none the less suggests that K2-260 b is likely among the class of more reflective hot Jupiters (e.g. Heng & Demory 2013; Sheets & Deming 2017).

The detection of a secondary eclipse that is dominated by reflected starlight also implies that there should in principle be a detectable phase curve in the optical. Our aggressive detrending procedure (Section 3.5) should have removed the phase curve from our phase-folded light curve, and indeed no phase variation is visible in Fig. 8. The detection of the phase curve, however, would be difficult, as it would require careful detrending of the stellar variability. This would be particularly complicated as the 2.16-d period that dominates the stellar variability (Section 3.4) is similar to the 2.63-d orbital period (which is why we used an aggressive detrending procedure in the first place). Such a detailed search for the phase curve is beyond the scope of this work.

4.5 Potential for further observations

Both K2-260 b and K2-261 b are promising targets for future observations to further characterize these systems. As discussed in Section 4.3, it is possible that K2-260 b has an orbit misaligned with respect to the stellar spin axis. Measuring the sky-projected component of this misalignment (λ) should be straightforward with either Rossiter–McLaughlin (e.g. Triaud et al. 2010) or Doppler tomographic (e.g. Johnson et al. 2017) observations. Given the properties of this system, we predict a Rossiter–McLaughlin semi-amplitude of $\sim$150 m s^{-1} for K2-260 b using the formulae of Gaudi & Winn (2007). K2-261 b is also a promising target for such observations, with a predicted Rossiter–McLaughlin amplitude of $\sim$7.5 m s^{-1}. Furthermore, the transit duration is relatively short for a long-period planet ($\sim$5 h), allowing a full transit to be observed in a single night, which is critical for RV Rossiter–McLaughlin observations. K2-260 b and K2-261 b are among the better *K2* targets for such observations; indeed, K2-260 b has the highest expected Rossiter–McLaughlin amplitude of any confirmed or validated *K2* planet orbiting a star brighter than $V = 15$. We show these objects' expected

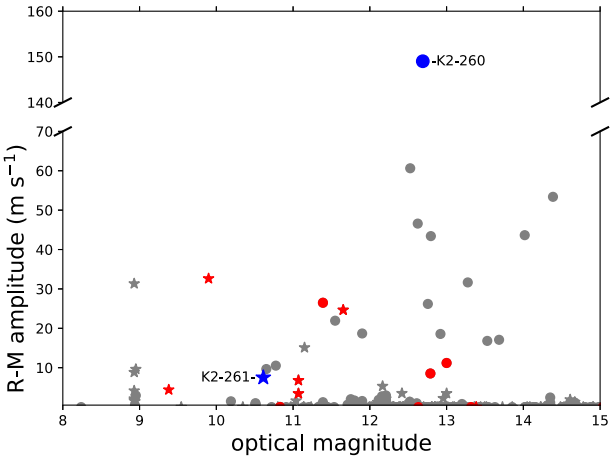

Figure 10. Predicted Rossiter–McLaughlin amplitude as a function of optical magnitude (either *V* or *Kp* depending upon the target) for transiting planets discovered by or observed by *K2*. Approximately, Saturn-sized planets ($0.5\ R_{\rm J} < R_P < 0.9\ R_{\rm J}$) are highlighted in black (red online), while K2-260 and K2-261 are shown in black (blue online) and are noted on the plot. Planets with $P < 10$ d are depicted as circles, while those with $P \geq 10$ d are depicted as stars. K2-261 is among the best Saturns and sub-Saturns, and one of the better long-period planets, for an obliquity measurement due to its combination of relatively large Rossiter–McLaughlin amplitude and bright host star. The axes are broken in order to better show K2-260 along with the rest of the population; no *K2* planets in the depicted magnitude range have expected R-M amplitudes between 70 and 140 m s^{-1}, and so the missing region of the plot is empty.

Rossiter–McLaughlin amplitudes in context with the remainder of the *K2* planet population in Fig. 10. These will require the use of large telescopes. As can be seen in Table 3, for K2-260 with FIES we are only able to obtain an RV precision of $\sim$60–150 m s^{-1} with 1-h exposures, which is insufficient to properly resolve the Rossiter–McLaughlin effect; ideally, one would need at least 8–10 exposures over the 4-h transit duration. For K2-261, we are able to obtain a per-point uncertainty of $\sim$1–3 m s^{-1} with $\sim$1200–1800 s exposures with HARPS or HARPS-N, which should be adequate to detect the Rossiter–McLaughlin effect; again, with FIES we are only able to obtain a per-point precision of $\sim$10 m s^{-1} with 3600-s exposures, insufficient to detect the Rossiter–McLaughlin effect for this target.

K2-261 is among the brightest stars to host a transiting giant planet with $P > 10$ d, which will facilitate other follow-up observations, in particular atmospheric transmission spectroscopy. Thanks to its relatively high temperature ($T_{\rm eq} = 1080^{+110}_{-100}$ K, assuming zero albedo and neglecting the orbital eccentricity) and low surface gravity ($\log g_P = 2.884^{+0.059}_{-0.072}$), we estimate a planetary atmospheric scale height of 580^{+110}_{-100} km, assuming a hydrogen-dominated atmosphere. For K2-260 b, we estimate a scale height of 550 ± 130 km, similar to K2-261 b as the higher planetary gravity largely offsets the higher equilibrium temperature. Although this is also reasonably favourable for transmission spectroscopy, at $V = 12.7$ these observations would be challenging simply because of the relative faintness of the host star.

Long-term RV monitoring of both systems could find or constrain the presence of additional planets in these systems. As discussed in Section 3.3 we found some evidence for a possible RV trend for K2-261, but rejected this possibility as it shifted the parameters of the transiting planet to imply an unphysical solution. Further observations could determine if there in fact might be another planet in the system, either by uncovering a long-term RV trend or finding

an RV periodicity due to a shorter-period planet. Our RV monitoring only spans ∼100 d for K2-260 and ∼130 d for K2-261, insufficient to detect any small, long-term trends.

5 CONCLUSIONS

We have presented the discovery, confirmation, and initial characterization of two transiting planets from *K2*, K2-260 b, and K2-261 b.

K2-260 b is a somewhat inflated hot Jupiter on a 2.6-d orbit around a mildly rapidly rotating ($v \sin i_\star = 16.0 \pm 2.0$ km s^{-1}) F6V star. We detect the secondary eclipse of the planet in the *Kepler* bandpass, which we find to be largely due to reflected starlight and use to estimate a planetary geometric albedo of $A_g \sim 0.2$. The host star also exhibits rotational modulation in its light curve. If the dominant periodicity of 2.16 d is the stellar rotation period then the planetary orbit must be misaligned with respect to the stellar rotation axis, as the predicted equatorial rotational velocity is much larger than the measured $v \sin i_\star$; if, however, the 2.16 -d periodicity is a harmonic of the true rotation period, then no large spin-orbit misalignment is required.

K2-261 b is a warm Saturn on an eccentric ($e = 0.39$), 11.6-d orbit around a bright ($V = 10.6$), metal-rich ([Fe/H] = +0.36) 8.8-Gyr-old G7 star at the main-sequence turn-off. The star is most likely a member of the Galactic thin disc, and is among the brightest stars to host a transiting giant planet with a period of greater than 10 d.

K2-260 b and K2-261 b add to the sample of transiting giant planets discovered by *K2*, and are both promising targets for follow-up observations to further characterize these systems. These could include observations of the Rossiter–McLaughlin effect (indeed, K2-260 b should have the largest Rossiter–McLaughlin amplitude of any planet discovered with *K2*), atmospheric transmission spectroscopy, and long-term RV monitoring.

During the revision process of this paper, we became aware of an independent discovery of K2-261 b by Brahm et al. (2018a). No information about this object, including on analysis and results, was shared between the two teams prior to the submission of either paper.

ACKNOWLEDGEMENTS

We thank the anonymous referee for helpful comments that improved the quality of the paper.

FD and JNW thank the Heising-Simons Foundation for financial support. Funding for the Stellar Astrophysics Centre is provided by The Danish National Research Foundation (Grant agreement no.: DNRF106). This research was partly supported by JSPS (Japan Society for the Promotion of Science) KAKENHI Grant Number JP18H01265 and JST (Japan Science and Technology Agency) PRESTO (Precursory Research for Embryonic Science and Technology) Grant Number JPMJPR1775, Japan. APH, SzCs, SG, JK, MP, and HR acknowledge support by DFG (Deutsche Forschungsgemeinschaft) grants HA 3279/12-1, PA525/18-1, PA525/19-1, PA525/20-1, and RA 714/14-1 within the DFG Schwerpunkt SPP 1992, 'Exploring the Diversity of Extrasolar Planets'. WDC, ME, and PJM acknowledge support from NASA (National Aeronautics and Space Administration) grants NNX16AJ11G and 80NSSC18K0447 to The University of Texas at Austin. MF and CMP gratefully acknowledge the support of the Swedish National Space Board. This project has received funding from the European Union's Horizon 2020 research and innovation programme under grant agreement no. 730890. This material reflects only the authors views, and the Commission is not liable for any use that may be made of the information contained therein.

We are very grateful to the McDonald, NOT, TNG, and ESO staff members for their support during the observations. This paper includes data taken at the McDonald Observatory of the University of Texas at Austin. Based on observations obtained (*a*) with the NOT, operated on the island of La Palma jointly by Denmark, Finland, Iceland, Norway, and Sweden, in the Spanish Observatorio del Roque de los Muchachos (ORM) of the Instituto de Astrofisica de Canarias (IAC), under programmes 56-010, 56-112, and 56-209; (*b*) with the Italian Telescopio Nazionale Galileo (TNG) also operated at the ORM (IAC) on the island of La Palma by the INAF (Istituto Nazionale di Astrofisica) – Fundacion Galileo Galilei, under Spanish CAT (Comisión de Asignación de Tiempos) programme CAT17B_99, OPTICON (Optical Infrared Coordination Network for Astronomy) programme OPT17B_59, and programme A36TAC_12, (*c*) with the 3.6 m ESO telescope at La Silla Observatory under programme 0100.C-0808 and 0101.C-0829. Based in part on data collected at Subaru Telescope, which is operated by the National Astronomical Observatory of Japan. The authors wish to recognize and acknowledge the very significant cultural role and reverence that the summit of Mauna Kea has always had within the indigenous Hawaiian community. We are most fortunate to have the opportunity to conduct observations from this mountain. This article is partly based on observations made with the MuSCAT2 instrument, developed by ABC (Astrobiology Center), at Telescopio Carlos Sánchez operated on the island of Tenerife by the IAC in the Spanish Observatorio del Teide. This work has made use of data from the European Space Agency (ESA) mission *Gaia* (https://www.cosmos.esa.int/gaia), processed by the *Gaia* Data Processing and Analysis Consortium (DPAC; https://www.cosmos.esa.int/web/gaia/dpac/consortium). Funding for the DPAC has been provided by national institutions, in particular the institutions participating in the *Gaia* Multilateral Agreement. This publication makes use of data products from the Wide-field Infrared Survey Explorer, which is a joint project of the University of California, Los Angeles, and the Jet Propulsion Laboratory/California Institute of Technology, funded by the National Aeronautics and Space Administration. This research made use of NASA's Astrophysics Data System and the NASA Exoplanet Archive, which is operated by the California Institute of Technology, under contract with the National Aeronautics and Space Administration under the Exoplanet Exploration Program. This research made use of ASTROPY, a community-developed core PYTHON package for Astronomy (Astropy Collaboration et al. 2013).

REFERENCES

Albrecht S. et al., 2012, ApJ, 757, 18
Astropy Collaboration et al., 2013, A&A, 558, A33
Baranne A. et al., 1996, A&AS, 119, 373
Blanco-Cuaresma S., Soubiran C., Heiter U., Jofré P., 2014, A&A, 569, A111
Borucki W. J. et al., 2010, Science, 327, 977
Brahm R. et al., 2018a, preprint (arXiv:1806.04073)
Brahm R. et al., 2018b, MNRAS, 477, 2572
Burke C. J. et al., 2015, ApJ, 809, 8
Cabrera J., Csizmadia S., Erikson A., Rauer H., Kirste S., 2012, A&A, 548, A44
Castelli F., Kurucz R. L., 2004, preprint (arXiv:0405087)
Chib S., Jeliazkov I., 2001, J. Am. Stat. Assoc., 96, 270
Claret A., 2004, A&A, 428, 1001
Collier Cameron A., Jardine M., 2018, MNRAS, 476, 2542

Cosentino R. et al., 2012, Proc. SPIE, 8446, 84461V
Coşkunolu B. et al., 2011, MNRAS, 412, 1237
Cutri R. M., et al., 2013, VizieR Online Data Catalog, 2328, 0
Dai F. et al., 2016, ApJ, 823, 115
Dai F. et al., 2017, AJ, 154, 226
Damiani C., Lanza A. F., 2015, A&A, 574, A39
Donati J. F. et al., 2008, MNRAS, 385, 1179
Doyle A. P., Davies G. R., Smalley B., Chaplin W. J., Elsworth Y., 2014, MNRAS, 444, 3592
Endl M., Cochran W. D., 2016, PASP, 128, 094502
Espinoza N. et al., 2017, MNRAS, 471, 4374
Esteves L. J., De Mooij E. J. W., Jayawardhana R., 2013, ApJ, 772, 51
Fabrycky D., Tremaine S., 2007, ApJ, 669, 1298
Foreman-Mackey D., Hogg D. W., Lang D., Goodman J., 2013, PASP, 125, 306
Frandsen S., Lindberg B., 1999, in Karttunen H., Piirola V., eds, Astrophysics with the NOT. University of Turku, Tuorla Observatory, Pikkio, Finland, p. 71
Fulton B. J., Petigura E. A., Blunt S., Sinukoff E., 2018, PASP, 130, 044504
Gaia Collaboration et al., 2016, A&A, 595, A1
Gaia Collaboration et al., 2018, A&A, 616, A1
Gandolfi D. et al., 2015, A&A, 576, A11
Gandolfi D. et al., 2017, AJ, 154, 123
Gaudi B. S., Winn J. N., 2007, ApJ, 655, 550
Girardi L., Groenewegen M. A. T., Hatziminaoglou E., da Costa L., 2005, A&A, 436, 895
Green G. M. et al., 2018, MNRAS, 478, 651
Grziwa S., Pätzold M., 2016, preprint (arXiv:1607.08417)
Grziwa S., Pätzold M., Carone L., 2012, MNRAS, 420, 1045
Grziwa S. et al., 2016, AJ, 152, 132
Hartig F., Minunno F., Paul S., 2017, BayesianTools: General-Purpose MCMC and SMC Samplers and Tools for Bayesian Statistics. https://github.com/florianhartig/BayesianTools
Hayano Y. et al., 2010, Proc. SPIE, 7736, 77360N
Heng K., Demory B.-O., 2013, ApJ, 777, 100
Hirano T. et al., 2016a, ApJ, 820, 41
Hirano T. et al., 2016b, ApJ, 825, 53
Howell S. B. et al., 2014, PASP, 126, 398
Huber D. et al., 2016, ApJS, 224:2
Huber K. F., Czesla S., Schmitt J. H. M. M., 2017, A&A, 597, A113
Johnson D. R. H., Soderblom D. R., 1987, AJ, 93, 864
Johnson M. C., Cochran W. D., Addison B. C., Tinney C. G., Wright D. J., 2017, AJ, 154, 137
Johnson M. C. et al., 2016, AJ, 151, 171
Johnson M. C. et al., 2018, AJ, 155, 100
Jódar E., Pérez-Garrido A., Díaz-Sánchez A., Villó I., Rebolo R., Pérez-Prieto J. A., 2013, MNRAS, 429, 859
Kipping D. M., 2013, MNRAS, 435, 2152
Kobayashi N. et al., 2000, in Iye M., Moorwood A. F., eds, Proc. SPIE Conf. Ser. Vol. 4008, Optical and IR Telescope Instrumentation and Detectors. SPIE, Bellingham, p. 1056
Kovács G., Zucker S., Mazeh T., 2002, A&A, 391, 369
Kraft R. P., 1967, ApJ, 150, 551
Kraus A. L., Hillenbrand L. A., 2007, AJ, 134, 2340
Kreidberg L., 2015, PASP, 127, 1161
Labadie L. et al., 2010, in Proc. SPIE Conf. Ser. Vol. 7735, Ground-based and Airborne Instrumentation for Astronomy III. SPIE, Bellingham, p. 77350X
Lanza A. F. et al., 2009, A&A, 506, 255
Lomb N. R., 1976, Ap&SS, 39, 447
Malavolta L. et al., 2018, AJ, 155, 107
Marshall D. J., Robin A. C., Reylé C., Schultheis M., Picaud S., 2006, A&A, 453, 635
Mayo A. W. et al., 2018, AJ, 155, 136
Mayor M. et al., 2003, Messenger, 114, 20
Mazeh T., Perets H. B., McQuillan A., Goldstein E. S., 2015, ApJ, 801, 3
McQuillan A., Mazeh T., Aigrain S., 2014, ApJS, 211, 24
Morton T. D., Bryson S. T., Coughlin J. L., Rowe J. F., Ravichandran G., Petigura E. A., Haas M. R., Batalha N. M., 2016, ApJ, 822, 86
Morton T. D., Johnson J. A., 2011, ApJ, 729, 138
Naoz S., Farr W. M., Rasio F. A., 2012, ApJ, 754, L36
Narita N. et al., 2017, PASJ, 69, 29
Narita N. et al., 2018, preprint (arXiv:1807.01908)
Ngo H. et al., 2016, ApJ, 827, 8
Niraula P. et al., 2017, AJ, 154, 266
Oscoz A. et al., 2008, Proc. SPIE, 7014, 701447
Pecaut M. J., Mamajek E. E., 2013, ApJS, 208, 9
Pepe F., Mayor M., Galland F., Naef D., Queloz D., Santos N. C., Udry S., Burnet M., 2002, A&A, 388, 632
Petigura E. A. et al., 2017, AJ, 153, 142
Pietrinferni A., Cassisi S., Salaris M., Castelli F., 2004, ApJ, 612, 168
Reddy B. E., Lambert D. L., Allende Prieto C., 2006, MNRAS, 367, 1329
Ricker G. R. et al., 2015, J. Astron. Telesc. Instrum. Syst., 1, 014003
Robin A. C., Reylé C., Derrière S., Picaud S., 2003, A&A, 409, 523
Scargle J. D., 1982, ApJ, 263, 835
Schlafly E. F., Finkbeiner D. P., 2011, ApJ, 737, 103
Sheets H. A., Deming D., 2017, AJ, 154, 160
Silva Aguirre V. et al., 2015, MNRAS, 452, 2127
Silva Aguirre V. et al., 2018, MNRAS, 475, 5487
Sing D. K., 2010, A&A, 510, A21
Sing D. K. et al., 2016, Nature, 529, 59
Smith A. M. S. et al., 2017, MNRAS, 464, 2708
Smith A. M. S. et al., 2018, MNRAS, 474, 5523
Sneden C., 1973, ApJ, 184, 839
Southworth J., 2015, Astrophysics Source Code Library, record ascl:1511.016
Telting J. H. et al., 2014, Astron. Nachr., 335, 41
Triaud A. H. M. J. et al., 2010, A&A, 524, A25
Tull R. G., MacQueen P. J., Sneden C., Lambert D. L., 1995, PASP, 107, 251
Uytterhoeven K. et al., 2011, A&A, 534, A125
Vanderburg A., Johnson J. A., 2014, PASP, 126, 948
Van Eylen V. et al., 2018, MNRAS, 478, 4866
Villanueva S. Jr. Gaudi B. S., Pogge R. W., Eastman J. D., Stassun K. G., Trueblood M., Trueblood P., 2018, PASP, 130, 015001
Winn J. N., Fabrycky D., Albrecht S., Johnson J. A., 2010, ApJ, 718, L145
Winn J. N. et al., 2017, AJ, 154, 270
Yu L. et al., 2018, preprint (arXiv:1803.02858)
Zechmeister M., Kürster M., 2009, A&A, 496, 577

[1]*Department of Astronomy, The Ohio State University, 140 West 18th Ave., Columbus, OH 43210, USA*
[2]*Department of Physics and Kavli Institute for Astrophysics and Space Research, Massachusetts Institute of Technology, Cambridge, MA 02139, USA*
[3]*Department of Astrophysical Sciences, Princeton University, 4 Ivy Lane, Princeton, NJ 08544, USA*
[4]*Stellar Astrophysics Centre, Department of Physics and Astronomy, Aarhus University, Ny Munkegrade 120, DK-8000 Aarhus C, Denmark*
[5]*Dipartimento di Fisica, Università di Torino, Via P. Giuria 1, I-10125 Torino, Italy*
[6]*Thüringer Landessternwarte Tautenburg, Sternwarte 5, D-07778 Tautenberg, Germany*
[7]*Departamento de Astrofísica, Universidad de La Laguna, E-38206 Tenerife, Spain*
[8]*Instituto de Astrofísica de Canarias, C/ Vía Láctea s/n, E-38205 La Laguna, Tenerife, Spain*
[9]*McDonald Observatory, University of Texas at Austin, 2515 Speedway, Stop C1400, Austin, TX 78712, USA*
[10]*Department of Astronomical Science, Graduate University for Advanced Studies (SOKENDAI), Mitaka, Tokyo 181-8588, Japan*
[11]*Department of Earth and Planetary Sciences, Tokyo Institute of Technology, 2-12-1 Ookayama, Meguro-ku, Tokyo 152-8551, Japan*

[12]*Institute for Astronomy, University of Hawaii, 2680 Woodlawn Drive, Honolulu, HI 96822, USA*
[13]*Department of Astronomy, The University of Tokyo, 7-3-1 Hongo, Bunkyo-ku, Tokyo 113-0033, Japan*
[14]*National Astronomical Observatory of Japan, NINS, 2-21-1 Osawa, Mitaka, Tokyo 181-8588, Japan*
[15]*Astrobiology Center, NINS, 2-21-1 Osawa, Mitaka, Tokyo 181-8588, Japan*
[16]*JST, PRESTO, 7-3-1 Hongo, Bunkyo-ku, Tokyo 113-0033, Japan*
[17]*Max-Planck-Institut für Astronomie, Königstuhl 17, D-69117 Heidelberg, Germany*
[18]*Astronomy Department and Van Vleck Observatory, Wesleyan University, Middletown, CT 06459, USA*
[19]*Institute of Planetary Research, German Aerospace Center, Rutherfordstrasse 2, D-12489 Berlin, Germany*
[20]*Rheinisches Institut für Umweltforschung, Abteilung Planetenforschung an der Universität zu Köln, Aachener Strasse 209, D-50931 Köln, Germany*
[21]*Department of Space, Earth and Environment, Chalmers University of Technology, Onsala Space Observatory, E-439 92 Onsala, Sweden*
[22]*Leiden Observatory, University of Leiden, PO Box 9513, NL-2300 RA Leiden, the Netherlands*
[23]*Department of Astronomy, Graduate School of Science, The University of Tokyo, Hongo 7-3-1, Bunkyo-ku, Tokyo 113-0033, Japan*
[24]*Nordic Optical Telescope, Rambla José Ana Fernández Pérez 7, E-38711 Breña Baja, Spain*
[25]*Dark Cosmology Centre, Niels Bohr Institute, University of Copenhagen, Juliane Maries Vej 30, 2100 Copenhagen Ø, Denmark*
[26]*Center for Astronomy and Astrophysics, TU Berlin, Hardenbergstr. 36, D-10623 Berlin, Germany*
[27]*Institut de Ciències de l'Espai (CSIC-IEEC), Carrer de Can Magrans, Campus UAB, E-08193 Bellaterra, Spain*

This paper has been typeset from a TEX/LATEX file prepared by the author.